JACS
JOURNAL OF THE AMERICAN CHEMICAL SOCIETY
Article
Cite This: J. Am. Chem. Soc. XXXX, XXX, XXX−XXX
pubs.acs.org/JACS

Cooperative Effects between Hydrophilic Pores and Solvents: Catalytic Consequences of Hydrogen Bonding on Alkene Epoxidation in Zeolites

Daniel T. Bregante,[†] Alayna M. Johnson,[†] Ami Y. Patel,[†] E. Zeynep Ayla,[†] Michael J. Cordon,[‡] Brandon C. Bukowski,[‡] Jeffrey Greeley,[‡] Rajamani Gounder,[‡] and David W. Flaherty*[,†]

[†]Department of Chemical and Biomolecular Engineering, University of Illinois at Urbana−Champaign, Urbana, Illinois 61801, United States

[‡]Charles D. Davidson School of Chemical Engineering, Purdue University, West Lafayette, Indiana 60208, United States

Supporting Information

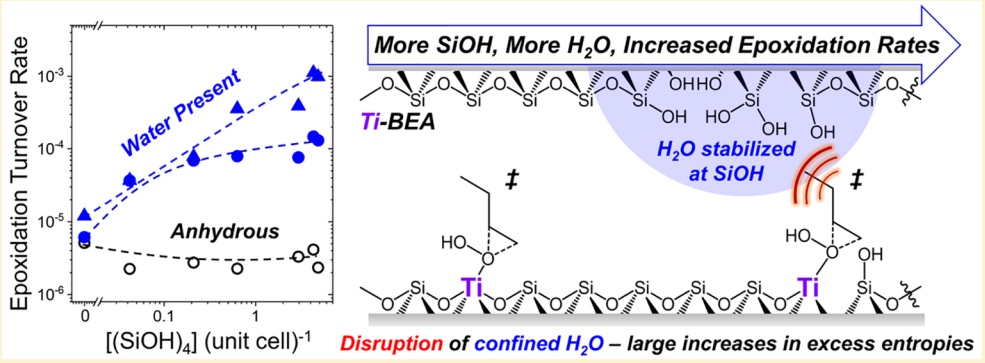

ABSTRACT: Hydrophobic voids within titanium silicates have long been considered necessary to achieve high rates and selectivities for alkene epoxidations with H_2O_2. The catalytic consequences of silanol groups and their stabilization of hydrogen-bonded networks of water (H_2O), however, have not been demonstrated in ways that lead to a clear understanding of their importance. We compare turnover rates for 1-octene epoxidation and H_2O_2 decomposition over a series of Ti-substituted zeolite *BEA (Ti-BEA) that encompasses a wide range of densities of silanol nests ($(SiOH)_4$). The most hydrophilic Ti-BEA gives epoxidation turnover rates that are 100 times larger than those in defect-free Ti-BEA, yet rates of H_2O_2 decomposition are similar for all $(SiOH)_4$ densities. These differences cause the most hydrophilic Ti-BEA to also give the highest selectivities, which defies conventional wisdom. Spectroscopic, thermodynamic, and kinetic evidence indicate that these catalytic differences are not due to changes in the electronic affinity of the active site, the electronic structure of Ti−OOH intermediates, or the mechanism for epoxidation. Comparisons of apparent activation enthalpies and entropies show that differences in epoxidation rates and selectivities reflect favorable entropy gains produced when epoxidation transition states disrupt hydrogen-bonded H_2O clusters anchored to $(SiOH)_4$ near active sites. Transition states for H_2O_2 decomposition hydrogen bond with H_2O in ways similar to Ti−OOH reactive species, such that decomposition becomes insensitive to the presence of $(SiOH)_4$. Collectively, these findings clarify how molecular interactions between reactive species, hydrogen-bonded solvent networks, and polar surfaces can influence rates and selectivities for epoxidation (and other reactions) in zeolite catalysts.

1. INTRODUCTION

Microporous catalytic materials (e.g., zeolites and zeotype structures) are of great industrial[1,2] and academic interest[3−6] because these catalysts provide the means to discriminate between reactants via shape selectivity and size exclusion[7] and to accelerate reactions and increase selectivities by stabilizing specific transition states.[8−10] Dispersive interactions with pore walls are largely responsible for the solvation of transition states (and other reactive intermediates) when the surrounding voids are vacant, such as found using gaseous reactants at high temperatures.[3,11] The number, variety, and complexity of interactions increase significantly when zeolite pores contain higher densities of reactive species or solvent molecules during catalysis in the liquid phase.[12] Specific interactions (e.g., hydrogen bonding, dipole interactions) between transition states, solvent molecules, and surface functions within pores are individually much weaker than the covalent and ionic bonds formed between reactive intermediates and active sites; however, the collective effects of weak specific forces can create extended (>1 nm) structures that surround catalytic active sites and reactive species.[13,14] These extended structures

Received: November 30, 2018

DOI: 10.1021/jacs.8b12861
J. Am. Chem. Soc. XXXX, XXX, XXX−XXX

reorganize to accommodate intermediates and transition states as reactions proceed and correspondingly contribute to the free-energy change associated with each elementary step along the reaction coordinate via changes in excess free energies (G^{ε}).

Solvent reorganization influences reactions within liquids promoted by homogeneous, enzymatic, or heterogeneous catalysts;[15−17] however, quantitative descriptions of these effects remain elusive, in particular, at the solid−liquid interface.[18,19] Many catalytic reactions (e.g., alkene epoxidation,[20−24] glucose isomerization,[12,25,26] Baeyer−Villiger oxidation[27]) at surfaces respond sensitively to the presence of water (H_2O), proximate hydroxyl groups, and hydrogen bonding even when these species exist at trace levels. The effects of H_2O and the associated hydrogen-bonded networks formed are particularly significant within the subnanometer pores of zeolite catalysts, which either preclude the formation of H_2O clusters when surfaces are nonpolar and hydrophobic or nucleate these same clusters when pore walls contain polar, hydrogen-bonding functions. Within the context of zeolite and zeotype catalysts, the densities of isolated silanol groups (SiOH) and of silanol nests ($(SiOH)_4$) within the material are known to have drastic effects on the adsorption properties and intrapore condensation of small molecules (e.g., H_2O,[28−31] CH_3OH,[25,31] C_2H_5OH[29,32]). Once stabilized within the pores, these species influence the stability of coadsorbates, reactive intermediates, and transition states through specific intermolecular interactions, such as hydrogen bonds. Unfortunately, the catalytic contributions of silanol groups and the networks of H_2O (or other solvents) they stabilize are not clear due to concomitant changes in other properties of the catalysts and reaction systems in previous investigations.

The role of hydrogen bonding within Ti-based zeolite catalysts on alkene epoxidation has been a topic of debate for decades.[21,22,24,33−38] Seminal studies on epoxidation within titanium silicalite-1 (TS-1) reported that the hydrophobic nature of pristine TS-1 gives greater yields of epoxide products with respect to hydrophilic titanium silicates (e.g., Ti-BEA, TiO_2−SiO_2), which was interpreted to be a consequence of increasing the concentration of the alkene substrate near active Ti active sites.[21,22,36] These foundational findings inspired a plethora of work on liquid-phase oxidations that sought to relate changes in the catalyst hydrophilicity to observed yields of oxidation products.[36−38] The reported differences in reactivity between TS-1 and other titanium silicates, however, likely reflect the convolution of transition-state confinement via dispersive interactions between pore walls and surface intermediates in addition to contributions related to the density and proximity of SiOH moieties. These results may also reflect different extents of intraparticle mass-transfer constraints because of variations in particle diameters and the strong dependence of effective diffusion coefficients on pore diameters.[39,40]

Recent studies that investigate the role of SiOH density in TS-1 specifically report epoxide yields that increase with expected densities of silanol groups, which directly contradict the conclusions described above.[24,35,37] For example, rates for epoxidation of 1-hexene are greater in TS-1 samples (relative to conventionally synthesized TS-1) with increased numbers of SiOH groups regardless of the method used to introduce these defects: crystallization in the presence of dimethyldimethoxysilane to produce geminal disilanols,[24] seeding with Al-doped TS-1 seeds to create a hierarchically structured material,[37] or the introduction of ethylenediamine to nucleate the formation of TiOH and SiOH defects.[35] In each of these studies, the authors conclude that the synthesis techniques changed either the electronic structure of the active sites[35] or the local concentrations of reactants;[24,37] however, these studies did not conclusively relate systematic differences in the catalyst structure to fundamental parameters for epoxidation catalysis. Recently, Grosso-Giordano et al. reported that initial turnover rates for cyclohexene epoxidation by *tert*-butyl hydroperoxide were five times greater at Ti active site (contained within a surface-grafted calix[4]arene) complexes grafted onto UCB-4 in comparison with the same Ti-calix[4]arene complex bound to MCM-41, which was attributed to consequential interactions between a proximate SiOH group and the Ti active sites on UCB-4 that facilitate either the activation of hydroperoxides or oxygen transfer to the alkene substrate via outer-sphere interactions mediated by the solvent.[41] Contradicting reports regarding hydrophobic effects in TS-1 and related Ti silicates, together with varied explanations for the origins of the differences in rates and yields, demonstrate the complexities of these systems and the difficulties in developing molecular interpretations of experimental results. Consequently, the catalysis community has not reached a consensus on the effects of SiOH groups and the associated hydrogen-bonded networks of solvent molecules on epoxidation catalysis, not to mention the fundamental origin of these effects and how they influence the stability of reactants and transition states.

Here we incorporate Ti atoms into the *BEA framework through postsynthetic modification of dealuminated *BEA and by hydrothermal synthesis to create a series of Ti-BEA catalysts with a wide range of silanol nest ($(SiOH)_4$) densities (0−5 $(SiOH)_4$ (unit cell)$^{-1}$) but with constant pore diameters and active Ti-site densities. We use this series of Ti-BEA to investigate the catalytic consequences of differences in only the density of $(SiOH)_4$ on turnover rates for 1-octene (C_8H_{16}) epoxidation and H_2O_2 decomposition, an undesirable parallel reaction pathway. Turnover rates of C_8H_{16} epoxidation are 100 times greater on Ti-BEA that contain ∼5 $(SiOH)_4$ (unit cell)$^{-1}$ than on defect-free materials. H_2O_2 decomposition rates, however, do not change with the density of $(SiOH)_4$. These large differences in epoxidation rates and H_2O_2 selectivities do not reflect differences in the electron affinities of the active sites, the identity of the active intermediates, or changes in the mechanism for epoxidation, all of which remain constant among the Ti-BEA catalysts within this study. Rather, the differences in epoxidation rates and the productive use of H_2O_2 among the Ti-BEA catalysts result from the short-range interactions between transition states for epoxidation (and H_2O_2 decomposition) with H_2O clusters that nucleate and bind to $(SiOH)_4$ in close proximity to the Ti active sites. These H_2O clusters stabilized by $(SiOH)_4$ exist in semiordered, hydrogen-bonded configurations within the pores of Ti-BEA. The formation of transition states for epoxidation requires that solvent molecules restructure to accommodate the activated complex. These changes disrupt stable hydrogen bonds and increase the entropy of the H_2O clusters in ways that overwhelm the associated enthalpy penalty. In contrast, transition states for H_2O_2 decomposition readily hydrogen bond and stabilize H_2O clusters, in ways reminiscent of the Ti−OOH species that saturate active sites, and thus show no discernible dependence on $(SiOH)_4$ density. Collectively, the findings presented here show that the excess free energies of the transition states for epoxidation are influenced by the

DOI: 10.1021/jacs.8b12861
J. Am. Chem. Soc. XXXX, XXX, XXX−XXX

density and proximity of $(SiOH)_4$ moieties and provide a quantitative relationship that describes the interaction of extended hydrogen-bonding structures with the transition states for epoxidation.

2. MATERIALS AND METHODS

2.1. Catalyst Synthesis. Ti-BEA-X, where X refers to the initial Si/Al ratio of the parent Al-BEA (X = 12.5−250), catalysts were prepared by postsynthetic modification of commercial Al-BEA samples (see Table 1 for manufacturer and initial Si/Al ratio).[42−47]

Table 1. Initial Si/Al Ratios, Metal Loadings, Band Gaps, and Fraction of Active Metal Atoms in Ti-BEA

sample name	zeolite vendor	initial Si/Al ratio[a]	Ti loading (wt %)[b]	band gap (eV)[c]	catalytically active Ti atoms (%)[d]
Ti-BEA-12.5	Zeolyst	12.5	0.20	4.2	102 ± 7
Ti-BEA-14	Tosoh	14	0.30	4.3	94 ± 6
Ti-BEA-20	Tosoh	20	0.34	4.3	97 ± 10
Ti-BEA-75	ACS Material	75	0.28	4.2	94 ± 7
Ti-BEA-150	Zeolyst	150	0.33	4.2	89 ± 7
Ti-BEA-250	Tosoh	250	0.42	4.2	93 ± 7
Ti-BEA-F	−	∞	0.15	4.3	92 ± 6

[a]Taken from technical data sheet supplied from manufacturer. [b]Measured by EDXRF. [c]Measured using DRUV−vis by extrapolating the linear portion of the leading edge in the corresponding Tauc plot. [d]Determined by in situ site titrations with methylphosphonic acid, where the rate measured as a function of MPA/Ti was extrapolated to a value of zero.

Al-BEA was treated in refluxing HNO_3 (Macron Chemicals, 68−70 wt %, 20 cm^3 g^{-1}; *Caution: HNO_3 is extremely caustic and will readily cause a chemical burn and should be handled carefully*) with the intent to remove framework Al atoms by forming soluble $Al(NO_3)_3$. The solids were then recovered by vacuum filtration and washed with H_2O (17.8 MΩ·cm, 50 cm^3 g^{-1}), followed by heating at 5 K min^{-1} in flowing air (100 cm^3 min^{-1}) and holding at 823 K for 6 h to remove residual volatile and organic species and to produce Si-BEA-X. Materials produced in this manner possessed Si/Al ratios >1400, as determined by energy-dispersive X-ray fluorescence spectroscopy. Ti atoms were incorporated by combining a stirred suspension of Si-BEA-X in CH_2Cl_2 (Fisher Chemicals, certified ACS stabilized) with an appropriate amount of $TiCl_4$ (Sigma-Aldrich, 99.9%; *Caution: $TiCl_4$ will violently react with moisture in the air to form HCl and should be handled carefully*) at reflux. All volatile components were then removed by rotary evaporation. The recovered solids were light brown, and these materials were treated by heating in flowing air (100 cm^3 min^{-1}) at 5 K min^{-1} and holding at 823 K for 6 h, which produced bright-white solid powders.

Ti-BEA-F was synthesized in fluoride media using a previously published procedure.[12,36] In brief, 4.89 g of tetraethylammonium fluoride (TEAF, Alfa Aesar, 97 wt %) was combined with 7.25 g of deionized H_2O (18.2 MΩ·cm) in a perfluoroalkoxy alkane (PFA) container (Savillex) with 10 g of tetraethylorthosilicate (TEOS, Sigma-Aldrich, >98 wt %) to form a gel. This gel was stirred for 1 h prior to the addition of 0.682 g of titanium(IV) isopropoxide (TIPO, Sigma-Aldrich, 99.999%), after which, the PFA container was sealed and the contents were stirred for 16 h at ambient temperature. The cover was then removed, and the excess ethanol, isopropanol, and water were allowed to evaporate at ambient temperature to yield a gel with a final molar composition of 1 SiO_2/0.008 TIPO/0.55 TEAF/7.15 H_2O. This gel was then loaded into a Teflon-lined stainless-steel autoclave (Parr instruments, 45 cm^3) and heated to 413 K while rotating (60 rpm) in a convection oven (Yamato, DKN-402C) for 25 days. The resultant solids were recovered, washed with H_2O and acetone (Sigma-Aldrich, >99.5 wt %) six times each (20 cm^3 g^{-1}), and dried for 16 h at 373 K. The dried solids were then heated in flowing air (1.67 cm^3 s^{-1} (g solids)$^{-1}$) at 853 K (1 K min^{-1}) for 10 h to produce a bleached-white solid.

2.2. Catalyst Characterization. The metal contents of Ti-BEA-X were determined using energy-dispersive X-ray fluorescence. In short, ∼30 mg of Ti-BEA was finely ground and loaded into a polypropylene sample holder (1 cm diameter) that was sealed with ultralene film. These were then loaded into a spectrometer (Shimadzu, EDX-7000), whose sample chamber compartment was purged with He (Airgas, ultrazero grade). Measurements were taken between 0 and 30 keV (100 scans), and the relative intensities of the fluorescence features for each element were used to calculate the mass of each element within the sample.

X-ray diffractograms of all Ti-BEA were obtained using a diffractometer (Siemens/Bruker, D5000) with Cu Kα radiation (0.15418 nm) under ambient conditions. Figure S1 shows the X-ray diffractograms of all Ti-BEA. The similarities between all diffractograms suggests that all Ti-BEA possess the *BEA zeolite framework.

Band-edge energies (E_g, Table 1) for each Ti-BEA were determined from extrapolation of the linear portion of the corresponding Tauc plot calculated from diffuse reflectance UV−vis spectra (DRUV−vis) (Figure S2). Total reflectance spectra were measured under ambient conditions with a UV−vis−NIR spectrophotometer (Agilent, CARY 5) with magnesium oxide (MgO, Sigma-Aldrich, 99.995%) as a solid diluent and background.

Solid-state magic-angle spinning−nuclear magnetic resonance (MAS NMR) spectroscopy was performed on a spectrometer (Varian, Unity Inova 300 MHz) equipped with a 4 mm MAS probe (Varian-Chemagnetics, double-resonance APEX HX) under ambient conditions. Prior to measurement, Ti-BEA was dehydrated in flowing He (100 cm^3 min^{-1}) at 573 K for 3 h. Ti-BEA was then loaded (∼35 mg) into a zirconia rotor that was spun at 10 kHz within the spectrometer. Powdered octakis(dimethylsilyloxy)silsesquioxane (Q_8M_8) was used for pulse calibration and ^{29}Si chemical shift referencing (Q_8M_8 has a chemical shift of 11.45 ppm). ^{29}Si direct polarization MAS NMR was performed with a 10 s recycle delay with the averaging of 8000 scans.

Infrared (IR) spectra of adsorbed CD_3CN (Cambridge Laboratories, 99.8% D atom) were obtained using a custom-built transmission cell[48] coupled to a Fourier transform infrared (FTIR) spectrometer (Bruker, Tensor 37) with a liquid-N_2-cooled HgCdTe detector. Catalysts were pressed into self-supporting disks (∼60 mg) and placed within the transmission cell, which was assembled using CaF_2 windows and connected to a gas manifold. All materials were first heated to 573 at 10 K min^{-1} and held for at least 3 h in flowing He (50 cm^3 min^{-1}; Airgas, ultrazero grade) with the intent to desorb water and volatile organics. CD_3CN was introduced via a syringe pump (KD Scientific, Legato 100) and vaporized in the gas-transfer lines into a stream of flowing He (50 cm^3 min^{-1}). Steady-state IR spectra (128 scans, 1 cm^{-1} resolution) of CD_3CN adsorbed to the M-BEA were obtained while flowing the CD_3CN/He stream over the samples.

Vapor-phase H_2O adsorption isotherms were collected on a volumetric adsorption instrument (Micromeritics, 3Flex). Ti-BEA samples (50−70 mg) were pelletized and sieved to retain particles between 250 and 500 μm in diameter. These were degassed by heating under vacuum (<7 × 10^{-4} kPa, 673 K) for 6 h prior to adsorption measurements. H_2O (17.8 MΩ·cm) was purified via one freeze−pump−thaw cycle prior to measurement.

The uptake of 1-octene (C_8H_{16}) was measured by combining Ti-BEA (∼10 mg) in a solution of C_8H_{16} (10^{-4} M C_8H_{16}, 0.039 M H_2O, 10 cm^3) with CH_3CN at 313 K. An initial (solids-free) aliquot was taken and analyzed via gas chromatography (GC; HP 5890, Series A) to determine the initial concentration of C_8H_{16}. Ti-BEA was then added to the stirring solution of C_8H_{16} and allowed to equilibrate at a given temperature. An aliquot of solution was then filtered (polypropylene, 0.22 μm) to remove the solids and was analyzed via GC. The adsorbed quantity was determined from the difference in GC peak area between the aliquot after the introduction of Ti-BEA and the initial sample.

2.3. Measurement of Rates for Epoxide Formation and H_2O_2 Decomposition. Rates for C_8H_{16} epoxidation and H_2O_2

DOI: 10.1021/jacs.8b12861
J. Am. Chem. Soc. XXXX, XXX, XXX−XXX

decomposition were measured using batch reactors (100 cm^3, three-necked round-bottomed flasks) equipped with reflux condensers to minimize evaporative losses. C_8H_{16} (Sigma-Aldrich, 98%), 5-hexen-1-ol ($C_6H_{12}O$; Sigma-Aldrich, 98%), *Z*-stilbene (Alfa-Aesar, 97%, 75:1 *Z*/*E* ratio), and H_2O_2 (Fischer Chemicals, 30 wt % in H_2O) or *tert*-butyl hydroperoxide (*t*-BuOOH; Sigma-Aldrich, 5.5 M in decane) were added to a solution of CH_3CN and benzene (internal standard for GC analysis; Sigma-Aldrich, thiophene-free, >99%) and heated to the desired temperature (303−348 K) while stirring at 700 rpm. The reactions were initiated by the addition of Ti-BEA, and small aliquots (~500 μL) of the reaction solution were extracted as a function of time through a syringe filter (0.22 μm, polypropylene). The concentrations of the organic components within these aliquots were quantified via a GC equipped with a flame-ionization detector. All species were identified, and calibration factors were quantified using standards of known concentration. The concentration of H_2O_2 in each aliquot was measured by colorimetric titration using an aqueous solution of $CuSO_4$ (8.3 mM, Fisher Chemicals, >98.6%), neocuproine (12 mM, Sigma-Aldrich, >98%), and ethanol (25% v/v, Decon Laboratories, 100%). The concentration of H_2O_2 was calculated by comparison of the absorbance at 454 nm to calibrated standards, measured on a spectrophotometer (Spectronic, 20 Genesys). In all reported data, the carbon balance closed within 95%, and the standard uncertainty for measured reaction rates was <10%. Rates for the conversion of C_8H_{16} and H_2O_2 were measured as functions of $[H_2O_2]$ and $[C_8H_{16}]$, and all reported results were obtained at differential conversion (i.e., <5% conversion of the limiting reagent). The identities of the products of 5-hexen-1-ol oxidation were confirmed using mass spectrometry. In short, liquid samples were injected into a gas chromatograph (Agilent, 6890N), and the resolved chromatographic features were subsequently analyzed in a mass spectrometer (Agilent, 5975B) using electron ionization techniques to determine the relevant mass-to-charge ratios.

The percent of active Ti atoms in each Ti-BEA was determined by in situ site titrations with methylphosphonic acid (MPA; Sigma-Aldrich, 99%) during the epoxidation of C_8H_{16} (0.01 M C_8H_{16}, 0.01 M H_2O_2, 313 K). In short, a suspension containing Ti-BEA (~30 mg), C_8H_{16}, benzene (as an internal standard), and MPA in CH_3CN was stirred for at least 1 h at 313 K with the intent to irreversibly bind MPA to active sites and inhibit epoxidation catalysis. Then, H_2O_2 was added to the reactor to initiate catalysis. Epoxidation rates were measured for systems with ratios of MPA/Ti ranging from zero to unity, and the number of active sites was determined by linear extrapolation of these data to determine the MPA/Ti ratio that gives a rate equal to zero (Figure S3).

2.4. Detection of Reactive Intermediates via In Situ UV−vis Spectroscopy. UV−vis spectra were collected using a 45° diffuse reflection probe (Avantes, solarization-resistant fibers) coupled to a fiber-optic spectrometer (Avantes, AvaFast 2048) with a compact deuterium-halogen light source (Avantes, AvaLight-DHc). Samples were pressed into 7 mm diameter pellets (~5 mg) and loaded into a liquid flow cell (~100 μL) with temperature control. Reactant and solvent solutions were introduced using a high-performance liquid chromatography pump (Waters, 515). Background UV−vis spectra (average of 100 scans) were obtained for each material by exposing the sample to a flowing CH_3CN solution (0.039 M H_2O, 1 cm^3 min^{-1}) at 313 K for 1 h. Spectra were obtained while flowing solutions of H_2O_2 in CH_3CN (0.1 M H_2O_2, 0.4 M H_2O, 1 cm^3 min^{-1}) at 313 K and continuing until the UV−vis spectra became constant, implying that the system reached steady-state. Displayed UV−vis spectra represent the difference between the experimental spectra and background spectra.

2.5. Computational Methods To Probe Interactions between CD_3CN and Adsorption Sites in Ti-BEA. Periodic, self-consistent density functional theory (DFT) using the Vienna Ab initio Simulation Package (VASP) was used to model the enthalpy and entropy of adsorption in zeolite BEA.[49−52] The computational details and unit-cell specifications were similar to those used previously to model ethanol dehydration in Sn-BEA.[53] In short, the Bayesian error estimation functional (BEEF-vdw) was used with projector augmented wave (PAW) pseudopotentials.[54−56] A plane-wave cutoff of 520 eV was used with a single gamma point and spin polarization. A force criterion of 20 meV/Å was used for geometric convergence. Optimized BEA unit-cell lattice constants were within 1.9% of those reported by the international zeolite database (IZA).[57]

Ab initio molecular dynamics (AIMD) simulations were performed with VASP at 350 K in an NVT ensemble using a Nosé−Hoover thermostat and a time step of 1 fs. CD_3CN was modeled within these AIMD simulations. Each MD simulation was equilibrated for at least 5 ps, followed by a 25 ps production run. Enthalpy changes ($\Delta H_{CD_3CN,x}$) were defined as an ensemble average of the AIMD energies (E) for gas-phase CD_3CN ($E_{CD_3CN(g)}$), the empty adsorption site (E_x), and CD_3CN interacting with adsorption site x ($E_{CD_3CN,x}$; e.g., Ti atoms)

$$\Delta H_{CD_3CN,x} = \langle E_{CD_3CN,x} \rangle - E_{CD_3CN(g)} - \langle E_x \rangle \quad (1)$$

where brackets denote an arithmetic averaging of accessible energies from the ensemble sampled by the thermostat.

The entropy of adsorbates was calculated using a two-phase thermodynamic model, which decomposes molecular trajectories into their translational, rotational, and vibrational degrees of freedom, expressed as the vibrational density of states (VDOS). Each VDOS was decomposed into its gaseous and solid components according to the original algorithm[58−60] and integrated to obtain entropies accounting for the plasticity of the BEA framework, as previously applied in the BEA framework for ethanol dehydration. The TRAVIS molecular trajectory code was used to analyze the calculated trajectories.[61] Estimates of the entropy loss upon physisorption involved calculating the principal root-mean-square fluctuations of CD_3CN from the AIMD trajectories.[62] Thus the entropy loss upon physisorption is predominantly caused by reduction in the translational degrees of freedom. The entropies of adsorption of CD_3CN on Ti and $(SiOH)_4$ defects were calculated as the differential changes in translational, rotational, and vibrational degrees of freedom relative to those calculated for the physisorbed state. This approach was necessary due to the difficulty in a direct AIMD method that describes absolute adsorption onto these sites from the gas phase. This, in part, may be due to the long time scales required to fully sample the relative translational and rotational modes available to gas-phase species. Thus, on Ti and $(SiOH)_4$ defects, the entropy change is modified by the nonrigid modes calculated by AIMD as compared with the nonrigid modes for physisorption, including the root-mean-square fluctuations.

The T8 crystallographic T-site of BEA was used to represent substitutional doping by Ti and $(SiOH)_4$. The T8 site was chosen based on previous reports of adsorbate stability at this site.[53] The Si atom occupying the T8 site was removed, and either the resulting vacancy was replaced with a Ti atom or the four framework oxygen atoms were bound by hydrogen atoms to simulate a $(SiOH)_4$ site. Isolated SiOH defects were not considered computationally because their formation at crystal grain boundaries and mesoscale defects precludes such sites from being constructed within a periodic unit cell. The simulated Si/Ti ratio within these calculations was 63:1, which corresponds to one Ti atom per unit cell.

3. RESULTS AND DISCUSSION

3.1. Quantifying the Density of Distinct Silanol Species with ^{29}Si MAS NMR and FTIR Spectroscopy. Ti-BEA-X (X = initial Si/Al ratio or F for hydrothermally synthesized) was synthesized through the postsynthetic modification of commercially available Al-BEA (initial Si/Al ~12.5−250) and through hydrothermal synthesis in fluoride media to prepare a suite of Ti-BEA with varying densities of $(SiOH)_4$ groups (Table 1). All Ti-BEA possess a single prominent UV−vis absorbance edge at ~300 nm that corresponds to the charge transfer from the 2p orbitals of oxygen to the 3d orbitals of Ti^{4+}.[63,64] This results in a band gap

DOI: 10.1021/jacs.8b12861
J. Am. Chem. Soc. XXXX, XXX, XXX−XXX

for Ti-BEA equal to 4.2 to 4.3 eV (Table 1; Figure S2). This suggests that the Ti-BEA used within this study contains highly disperse Ti atoms and few TiO_x oligomers or larger aggregates. The number of catalytically active sites was determined by in situ site titrations with MPA (Section 2.3). Titrations with MPA show that turnover rates decrease linearly as a function of the molecular ratio of MPA/Ti for all Ti-BEA (Figure S3) and that rates become immeasurable when the MPA/Ti ratio approaches unity. These data suggest that nearly all Ti atoms form active sites, and the linearity of these titrations indicates that rates of epoxidations at all active sites are approximately equal within a given Ti-BEA catalyst. The combined results of titrations with MPA and the interpretations of band gaps measured via UV−vis support the conclusion that Ti atoms are highly dispersed within the Ti-BEA samples.

The fraction of Si atoms coordinated to −OH groups (i.e., SiOH) within each Ti-BEA material was estimated using ^{29}Si solid-state MAS NMR spectroscopy. Figure 1 shows that ^{29}Si MAS NMR spectra contain distinct NMR features at chemical shifts of −102, −112, −113, and −116 ppm on dehydrated Ti-BEA-14, Ti-BEA-75, Ti-BEA-250, and Ti-BEA-F. (^{29}Si NMR spectra for all Ti-BEA are shown in Figure S4.) The feature at −102 ppm corresponds to Si atoms that possess a single pendant hydroxyl moiety (i.e., $Si(OSi)_3(OH)$, denoted as Q^3 sites),[65,66] and peaks at −112, −113, and −116 ppm originate from Si atoms within the framework of *BEA coordinated to four siloxane functions (i.e., $Si(OSi)_4$, denoted as Q^4 sites). The splitting among these Q^4 sites reflects contributions from the nine crystallographically distinct tetrahedral sites of *BEA, which are clearly resolved in materials with the greatest degree of crystallinity (e.g., Ti-BEA-F). The ratio of the peak areas for the Q^3 sites to the sum of those for the Q^3 and Q^4 sites (Φ_{NMR}) provides a quantitative measure of the fraction of Si atoms that reside as SiOH functions

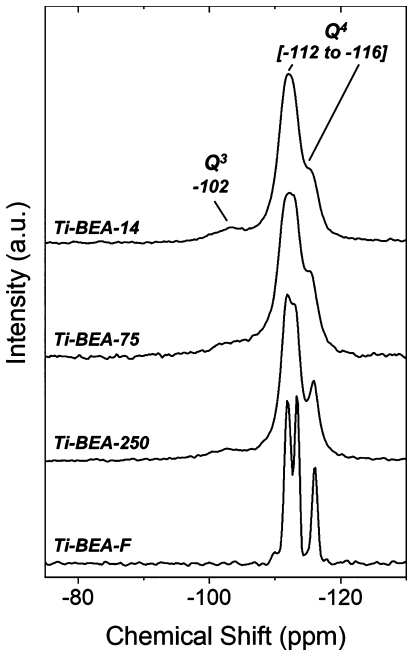

Figure 1. ^{29}Si direct polarization MAS NMR of Ti-BEA-14, Ti-BEA-75, Ti-BEA-250, and Ti-BEA-F. Spectra are normalized to the Q^4 feature and are vertically offset for clarity.

$$\Phi_{NMR} = \frac{A_{Q^3}}{A_{Q^3} + A_{Q^4}} \quad (2)$$

where A_{Q_3} and A_{Q_4} represent the areas of the deconvoluted ^{29}Si NMR features for Q^3 and Q^4 sites, respectively. (Section S1 shows ^{29}Si NMR spectra for all Ti-BEA and representative peak fits used to calculate values of Φ_{NMR} (Figure S5).) Table 2 shows that Φ_{NMR} decreases systematically as the initial ratio of Si/Al increases for postsynthetically modified Ti-BEA catalysts and is nearly zero for Ti-BEA-F. Notably, Φ_{NMR} does not represent the density of $(SiOH)_4$ groups (i.e., $[(SiOH)_4]$) because isolated silanol groups (e.g., on the external surface of Ti-BEA particles) also contribute to the Q^3 feature. Consequently, clear relationships between the number of $(SiOH)_4$ and fundamental quantities that determine turnover rates and selectivities for epoxidations in these catalysts require a more specific measure of the $[(SiOH)_4]$ for each material.

IR spectra of *BEA catalysts contain distinct ν(O−H) modes between 3300 and 3750 cm^{-1} that can be deconvoluted into semiquantitative estimates for the number of isolated and hydrogen-bonded (e.g., $(SiOH)_4$) silanol groups.[27,47,67] Figure 2 shows IR spectra of Ti-BEA-14, Ti-BEA-75, Ti-BEA-250, and Ti-BEA-F after treatments that desorb adventitious H_2O. (IR spectra for all Ti-BEA are shown in Figure S6.) These spectra show distinct features at 1990 and 1865 cm^{-1} that reflect ν(Si−O−Si) overtones (i.e., contributions from the *BEA framework) and between 3300 and 3750 cm^{-1}, which correspond to ν(O−H) modes of distinct SiOH species.[27,67,68]

Table 2. Fraction of Si Atoms Existing as SiOH (Φ_{NMR}), Relative Densities of Hydrogen-Bonded SiOH (Φ_{IR}), Adsorption Enthalpies for CD_3CN Bound to Ti Atoms ($\Delta H_{CD_3CN,Ti}$) and of Ti-(η^2-O_2) and Ti−OOH, and *Z*/*E* Ratios for the Epoxidation of *Z*-Stilbene over Ti-BEA

sample name	Φ_{NMR} [a]	Φ_{IR} [b]	$\Delta H_{CD_3CN,Ti}$ (kJ mol^{-1}) [c]	Ti−OOH LMCT energy (eV) [d]	Ti-(η^2-O_2) LMCT energy (eV) [d]	*Z*/*E* ratio *Z*-stilbene [e]
Ti-BEA-12.5	0.062	2.30	−32 ± 1	3.1	3.6	14 ± 2
Ti-BEA-14	0.055	2.52	−29 ± 2	3.1	3.5	10 ± 3
Ti-BEA-20	0.052	1.90	−30 ± 1	3.0	3.6	9 ± 2
Ti-BEA-75	0.056	2.21	−31 ± 2	3.1	3.7	11 ± 4
Ti-BEA-150	0.047	1.64	−30 ± 2	2.9	3.6	6 ± 2
Ti-BEA-250	0.041	1.26	−28 ± 1	3.0	3.6	5 ± 1
Ti-BEA-F	∼0	0.08	−32 ± 1	3.1	3.8	7 ± 2

[a]Determined from ^{29}Si NMR spectra of dehydrated Ti-BEA. [b]Determined from FTIR spectra of dehydrated Ti-BEA. [c]Corresponds to CD_3CN bound to Ti atoms, determined from adsorption isobars using FTIR. [d]Determined from in situ UV−vis (0.01 M H_2O_2 in CH_3CN, 313 K). [e]Calculated from product selectivities of *Z*-stilbene epoxidation (1 mM *Z*-stilbene, 0.01 M H_2O_2 in CH_3CN, 313 K).

DOI: 10.1021/jacs.8b12861
J. Am. Chem. Soc. XXXX, XXX, XXX−XXX

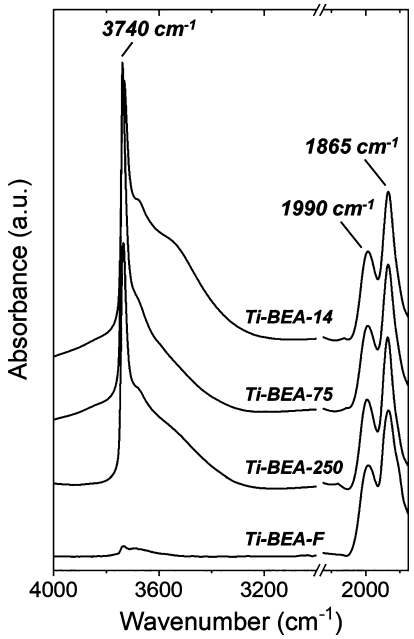

Figure 2. Infrared spectra of dehydrated Ti-BEA-14, Ti-BEA-75, Ti-BEA-250, and Ti-BEA-F (50 cm^3 min^{-1} He, 573 K). All spectra are normalized to the ν(Si−O−Si) overtone at 1865 cm^{-1}, assumed to have a constant extinction coefficient for all Ti-BEA. Spectra are vertically offset for clarity.

The sharp peak at 3740 cm^{-1} corresponds to the ν(O−H) of isolated SiOH groups that do not hydrogen bond or interact with other species (i.e., crystal defects within the zeolite or SiOH on the surface of the zeolite particle). The broad feature extending from 3300 to 3750 cm^{-1} reflects $(SiOH)_x$ groups (e.g., $(SiOH)_4$) that contain proximate, hydrogen-bonded −OH functions.[47,69] The most hydrophilic Ti-BEA contains multiple $(SiOH)_4$ groups per unit cell, which suggests that a significant fraction of these $(SiOH)_4$ groups will be paired with another and may lead to a greater extent of hydrogen bonding (i.e., resulting in the bimodal character of ν(O−H) within hydrophilic Ti-BEA).

Differences in the density of isolated SiOH and $(SiOH)_4$ groups on each material across the series of Ti-BEA are determined by normalizing spectra by the intensity of the ν(Si−O−Si) modes (i.e., assuming a constant density of framework Si−O−Si bonds) and deconvoluting the peaks for SiOH (3740 cm^{-1}) and $(SiOH)_4$ groups (3300−3700 cm^{-1}), as shown in the SI (Figure S7). The ratios of the integrated areas (Φ_{IR}) for ν(O−H) of $(SiOH)_4$ ($A_{(SiOH)_4}$) to those for ν(Si−O−Si) ($A_{(Si-O-Si)}$) provide measures of the relative density of $(SiOH)_4$ for each Ti-BEA

$$\Phi_{IR} = \frac{A_{(SiOH)_4}}{A_{(Si-O-Si)}} \quad (3)$$

Table 2 shows that values for Φ_{IR} decrease as the initial ratio of Si/Al increases in the parent BEA zeolites, which is consistent with the trends observed for the total number of Si atoms coordinated to −OH groups (shown by Φ_{NMR}). Φ_{IR}, as defined here, provides a semiquantitative measure for changes in the number of $(SiOH)_4$ groups that result from differences in synthesis protocols for a given zeolite framework; however, comparisons between different zeolite frameworks require values for extinction coefficients because these likely vary for ν(Si−O−Si) modes across structures.

Figure 3 shows isotherms for the adsorption of H_2O as functions of relative H_2O pressures (P/P_0) onto Ti-BEA-14,

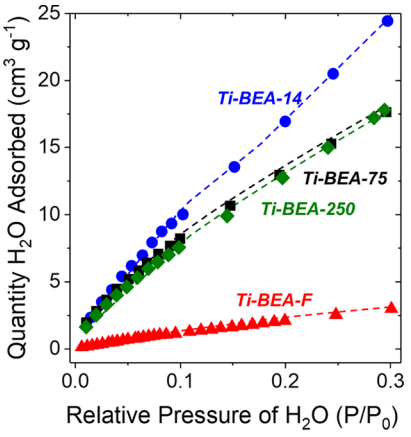

Figure 3. H_2O adsorption isotherms for Ti-BEA-14 (blue ●), Ti-BEA-75 (■), Ti-BEA-250 (green ◆), and Ti-BEA-F (red ▲) at 293 K. Dashed curves are intended to guide the eye.

Ti-BEA-75, Ti-BEA-250, and Ti-BEA-F, and notably the uptake of H_2O onto Ti-BEA-F is much smaller than that for Ti-BEA synthesized by postsynthetic modification at P/P_0 values below 0.3. (Adsorption isotherms for all Ti-BEA are shown in Figure S8.) At low values of P/P_0 (i.e., <0.05), H_2O adsorbs to SiOH and $(SiOH)_4$, which appear as nearly identical uptakes among Ti-BEA synthesized by postsynthetic modification. Ti-BEA-F, however, adsorbs significantly less H_2O at all P/P_0 as this material does not contain sufficient densities of SiOH or $(SiOH)_4$ to nucleate the formation of stable H_2O clusters. Notably, H_2O cluster formation upon adsorption occurs via stabilizing hydrogen-bonding interactions with SiOH and $(SiOH)_4$, as observed experimentally and computationally for zeolites with the MFI framework.[28−30] H_2O molecules bind exothermically to monomeric, dimeric, or oligomeric H_2O clusters with adsorption enthalpies of approximately −33 kJ mol^{-1},[70] which indicates that small H_2O clusters form spontaneously within Ti-BEA following the stable coordination of a few molecules to silanol defects. This suggests that H_2O adsorption cannot capture nuanced differences in the density of SiOH groups, whose quantification requires spectroscopic interrogation (see above).

3.2. Identifying Chemically Distinct Binding Sites within Ti-BEA by Adsorption of CD_3CN. IR spectra of CD_3CN adsorbed onto Ti-BEA were used to determine the adsorption enthalpies and entropies of distinguishable adsorption sites, including Ti atoms, SiOH or $(SiOH)_4$ groups, and siloxane regions of the pore walls (denoted as Si−O−Si)[25,71] and to compare electron affinities of Ti-active sites in Ti-BEA. Figure 4a,b shows IR spectra obtained during adsorption isotherms of CD_3CN onto Ti-BEA-12.5 and Ti-BEA-F, respectively. The absorbance features at 2263, 2274, and 2302 cm^{-1} correspond to the ν(C≡N) of CD_3CN molecules physisorbed to Si−O−Si, adsorbed to SiOH and $(SiOH)_4$ functions, and bound to Lewis acidic framework Ti atoms, respectively.[42,71,72] Features at 2215 and 2115 cm^{-1} correspond to $\nu_{as}(CD_3)$ and $\nu_s(CD_3)$, respectively.[42] The areas of the ν(C≡N) absorbance bands for CD_3CN ($A_{\nu(C\equiv N),x}$)

DOI: 10.1021/jacs.8b12861
J. Am. Chem. Soc. XXXX, XXX, XXX−XXX

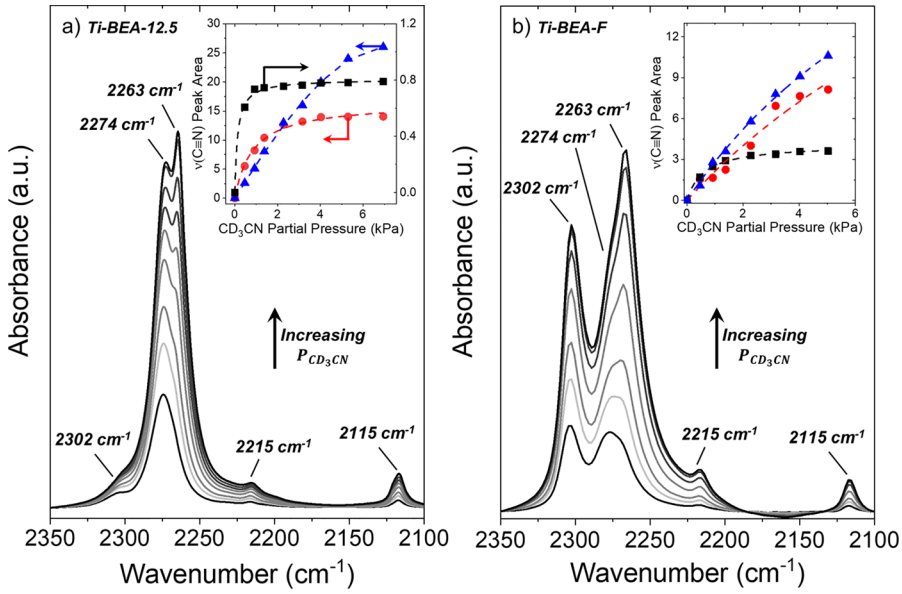

Figure 4. Infrared spectra of equilibrium coverages of adsorbed CD_3CN on (a) Ti-BEA-12.5 (0.46−6.95 kPa CD_3CN, 346 K) and (b) Ti-BEA-F (0.46−5.03 kPa CD_3CN, 387 K). The inset shows peak areas of the $\nu(C{\equiv}N)$ IR absorbance features for CD_3CN bound to SiOH and $(SiOH)_4$ groups (red ●), Ti atoms (■), and Si−O−Si (blue ▲). Dashed lines represent least-squares regression fits of eq 5.

Table 3. Adsorption Enthalpies and Entropies for CD_3CN Bound to Lewis Acidic Ti Atoms, to $(SiOH)_x$ Moieties, and to Si−O−Si on Ti-BEA-12.5 and Ti-BEA-F

sample	$\Delta H_{CD_3CN,Ti}$ (kJ mol^{-1})	$\Delta H_{CD_3CN,(SiOH)_x}$ (kJ mol^{-1})[a]	$\Delta H_{CD_3CN,Si-O-Si}$ (kJ mol^{-1})	$\Delta S_{CD_3CN,Ti}$ (J mol^{-1} K^{-1})	$\Delta S_{CD_3CN,(SiOH)_x}$ (J mol^{-1} K^{-1})[a]	$\Delta S_{CD_3CN,Si-O-Si}$ (J mol^{-1} K^{-1})
Ti-BEA-12.5	−32 ± 1	−55 ± 4	−[b]	−83 ± 5	−150 ± 10	−[b]
Ti-BEA-F	−32 ± 1	−19 ± 1	−12 ± 1	−99 ± 10	−87 ± 6	−75 ± 8
DFT model[c]	−20	−41[d]/−33[e]	−22	−85	−117[d]/−134[e]	−67

[a]Subscript x is equal to either 1 (for Ti-BEA-F) or 4 (for Ti-BEA-12.5 and within the DFT model) to denote isolated SiOH or $(SiOH)_4$, respectively. [b]CD_3CN physisorbed to Ti-BEA-12.5 was not spectroscopically observable at the pressure (0.46 kPa) and temperatures (373−423 K) used for van't Hoff analysis. [c]Estimated by ab initio molecular dynamics at 350 K with one Ti or $(SiOH)_4$ per unit cell. [d]Corresponds to the adsorption of CD_3CN onto $(SiOH)_4$. [e]Corresponds to the adsorption of three CD_3CN per $(SiOH)_4$ nest.

bound to SiOH moieties, Ti atoms, and Si−O−Si are assumed to be proportional to their fractional coverage ($\theta_{CD_3CN,x}$).

$$\theta_{CD_3CN,x} = \frac{A_{\nu(C{\equiv}N),x}}{A_{\nu(C{\equiv}N),sat}} \quad (4)$$

where $A_{\nu(C{\equiv}N),sat}$ is the area of the $\nu(C{\equiv}N)$ feature for CD_3CN bound to a given adsorption site x (i.e., SiOH, Ti, or Si−O−Si) at saturation coverage.

The increases in $\theta_{CD_3CN,x}$ with the partial pressure of CD_3CN (P_{CD_3CN}) at each of the three chemically distinct locations (insets of Figure 4a,b) are each consistent with the functional form of a Langmuirian adsorption isotherm[39] represented by

$$\theta_{CD_3CN,x} = \frac{K_x P_{CD_3CN}}{1 + K_x P_{CD_3CN}} \quad (5)$$

where K_x is the equilibrium coefficient for CD_3CN adsorption onto adsorption site x. A representative peak-fitting procedure to determine these areas is given in Section S2.1. The close agreement between the Langmuirian model and the measured coverages suggests that all adsorption locations within each category of sites are chemically similar and that adsorbed CD_3CN molecules do not interact significantly with one another under these conditions. Consequently, enthalpies ($\Delta H_{CD_3CN,x}$) and entropies ($\Delta S_{CD_3CN,x}$) for the adsorption of CD_3CN to a given site x are determined from values of K_x following the van't Hoff approach

$$K_x = e^{(-\Delta H_{CD_3CN,x}/RT)} e^{(\Delta S_{CD_3CN,x}/R)} \quad (6)$$

Table 3 shows values of $\Delta H_{CD_3CN,x}$ and $\Delta S_{CD_3CN,x}$ for CD_3CN bound to Ti atoms, SiOH, and Si−O−Si on Ti-BEA-12.5 and Ti-BEA-F, measured experimentally (0.46 kPa CD_3CN, 373−423 K, Figure S10) and calculated from AIMD simulations. Experimental values of $\Delta H_{CD_3CN,Ti}$ and $\Delta S_{CD_3CN,Ti}$ do not differ between Ti-BEA-12.5 and Ti-BEA-F within the measured uncertainty, which suggests that the density or proximity of SiOH and $(SiOH)_4$ groups does not influence the coordination and stability of CD_3CN bound to framework Ti atoms. The value of $\Delta S_{CD_3CN,Ti}$ calculated by AIMD agrees closely with the experimental values of $\Delta S_{CD_3CN,Ti}$ (−85 versus −83 to −99 J mol^{-1} K^{-1}); however, values of $\Delta H_{CD_3CN,Ti}$ estimated from AIMD are lower (−20 versus −32 kJ mol^{-1}) than those measured experimentally.

Molecules of CD_3CN physisorb to Si−O−Si pore walls more weakly than to Ti atoms ($\Delta H_{CD_3CN,Si-O-Si}$ = −12 kJ mol^{-1} versus $\Delta H_{CD_3CN,Ti}$ = −32 kJ mol^{-1}), as expected because the adsorption of CD_3CN to Ti atoms involves specific Lewis acid−base interactions. As a result, entropy losses upon

DOI: 10.1021/jacs.8b12861
J. Am. Chem. Soc. XXXX, XXX, XXX−XXX

binding to siloxane regions are also smaller than those for Ti atoms ($\Delta S_{CD_3CN,Si-O-Si}$ = −75; $\Delta S_{CD_3CN,Ti}$ = −83 to −99 J mol^{-1} K^{-1}). The measured entropy lost upon adsorption to Si−O−Si is similar to estimates from AIMD simulations (−75 versus −67 J mol^{-1} K^{-1}). Yet calculated values of $\Delta H_{CD_3CN,Si-O-Si}$ are significantly larger than those measured (−22 versus −12 kJ mol^{-1}) and are identical to calculated values of $\Delta H_{CD_3CN,Ti}$. These systematic discrepancies between measured and calculated adsorption enthalpies likely reflect errors in the functional used to assess weak Lewis acid−base interactions. Notably, however, these calculations do seem to describe accurately the entropy for adsorption of CD_3CN to Si−O−Si and Ti sites.

Ti-BEA-F contains primarily isolated SiOH that forms through stochastic processes that introduce crystallographic defects during hydrothermal synthesis. Molecules of CD_3CN adsorb more weakly onto SiOH within Ti-BEA-F than $(SiOH)_4$ within Ti-BEA-12.5 ($\Delta H_{CD_3CN,SiOH}$ = −19 kJ mol^{-1}; $\Delta H_{CD_3CN,(SiOH)_4}$ = −31 kJ mol^{-1}). Moreover, CD_3CN bound to $(SiOH)_4$ within Ti-BEA-12.5 possesses lower entropies than CD_3CN adsorbed to SiOH within Ti-BEA-F ($\Delta S_{CD_3CN,(SiOH)_4}$ = −150 J mol^{-1} K^{-1}; $\Delta S_{CD_3CN,SiOH}$ = −87 J mol^{-1} K^{-1}). Notably, values of $\Delta S_{CD_3CN,SiOH}$ are similar to those of $\Delta S_{CD_3CN,Ti}$ because CD_3CN, when bound to isolated SiOH, is oriented into the pore of *BEA and likely possesses similar vibrational entropic modes (e.g., frustrated translation, hindered rotation). As mentioned above, we did not investigate AIMD simulations for the interaction of CD_3CN with isolated SiOH because the exact structure of these isolated defects within *BEA is not known.

AIMD simulations for a single CD_3CN adsorbed to $(SiOH)_4$ show similar enthalpic stabilities to those measured ($\Delta H_{CD_3CN,(SiOH)_4}$ = −41 versus −55 kJ mol^{-1}) yet underestimate the entropy lost upon adsorption ($\Delta S_{CD_3CN,(SiOH)_4}$ = −117 versus −150 J mol^{-1} K^{1-}). It is possible, however, that silanol nests may stabilize the adsorption of multiple adsorbates, as the adsorption geometries of molecules onto $(SiOH)_4$ have not previously been elucidated. Indeed, the adsorption of three CD_3CN molecules to $(SiOH)_4$ results in AIMD-derived $\Delta H_{CD_3CN,(SiOH)_4}$ values that are similar to those predicted for a single CD_3CN molecule, suggesting that there is minimal enthalpic change (per molecule) for the adsorption of one or multiple CD_3CN to $(SiOH)_4$. Furthermore, the adsorption of three CD_3CN molecules onto $(SiOH)_4$ does, in fact, show average entropies lost upon adsorption that are similar to those measured (−134 versus 150 J mol^{-1} K^{-1}).

The representative geometries for CD_3CN bound to $(SiOH)_4$ (Figure S12d) show that a molecule of CD_3CN is projected perpendicularly to the 12-membered pore of *BEA in a vacancy produced from $(SiOH)_4$. The peak position of $\nu_s(-CD_3)$ is blue-shifted with increasing $\theta_{CD_3CN,(SiOH)_4}$ (Figure S11), which reflects the interaction between the $-CD_3$ moiety and an electron-rich moiety (e.g., the −OH in $(SiOH)_4$).[73] This shift in $\nu_s(-CD_3)$ supports the results from AIMD, which suggest that CD_3CN may adsorb into $(SiOH)_4$ perpendicular to the main pore of *BEA in the space afforded from $(SiOH)_4$. The adsorption of CD_3CN perpendicular to the 12-membered ring of *BEA primarily results in a significant loss of rotational entropy. This interpretation (i.e., the loss in rotation entropy) is also supported by estimates for entropies of adsorption, calculated using the model of Campbell et al. (eq S1, Section S2.2).[74]

The differences in $\Delta S_{CD_3CN,(SiOH)_4}$ and $\Delta S_{CD_3CN,Ti}$ primarily reflect the differences in the frustrated translational and hindered rotational entropy of CD_3CN adsorbed to $(SiOH)_4$ or Ti atoms, respectively. Decomposition of the translational and rotational contributions to the adsorbate entropy within the AIMD simulations (Table S1) shows that the difference between $\Delta S_{CD_3CN,(SiOH)_4}$ and $\Delta S_{CD_3CN,Ti}$ is consistent with the difference in rotational entropy of CD_3CN bound to Ti atoms versus $(SiOH)_4$. The entropy of CD_3CN bound to Ti atoms and $(SiOH)_4$ was also estimated using the Sackur−Tetrode equation and the corresponding partition functions that describe frustrated translation and hindered rotation in Section S2.3 (Table 1). Estimates for the entropy of hindered rotations of CD_3CN bound to Ti provide a value of 40 J mol^{-1} K, when the maximum degree of rotation is assumed to be 40°. This estimate compares favorably to the measured difference in adsorption entropies determined experimentally (65 ± 10 kJ mol^{-1}) and predicted from AIMD simulations (49 kJ mol^{-1} K^{-1}) for CD_3CN bound to $(SiOH)_4$ in comparison with Ti sites, which further suggests that the adsorption of CD_3CN onto $(SiOH)_4$ results in the strong interaction of CD_3CN with the side channel afforded by $(SiOH)_4$.

Values of $\Delta H_{CD_3CN,Ti}$ reflect the formation of a Lewis acid−base adduct and may seem small in comparison with $\Delta H_{CD_3CN,SiOH}$; however, the strength of these interactions is consistent with measured heats of reaction for complexes of CH_3CN and homogeneous Lewis acids.[75−77] For example, $SbCl_5$ is used for comparisons of Lewis acidity,[78] and the heat of formation of the $CH_3CN-SbCl_5$ is −59 kJ mol^{-1} (in dichloroethane).[75] Moreover, $SbCl_5$ is a stronger Lewis acid than Ti alkoxides (e.g., $Ti(OiPr)_4$), which may possess electron affinities similar to framework Ti atoms in Ti-BEA. As such, the measured values of $\Delta H_{CD_3CN,Ti}$ on Ti-BEA-12.5 and Ti-BEA-F seem reasonable, and differences between these zeolitic materials arise predominantly in the density and types of SiOH or $(SiOH)_4$ sites.

In summary, the principal differences between the Ti-BEA samples do not reflect differences between the electronic properties (i.e., electron affinity) of the active sites among these materials; therefore, any catalytic differences that may arise must relate to differences in the properties of the active intermediates (Section 3.3), mechanism for epoxidation (Section 3.4), or density of $(SiOH)_4$ (Section 3.5).

3.3. Identity and Electronic Properties of Reactive Species Formed Upon H_2O_2 Activation. Comparisons of steady-state UV−vis spectra of Ti-BEA in contact with solutions of H_2O_2 were used to determine if differences in the $[(SiOH)_4]$ lead to changes in the identity or electronic properties of the reactive surface species formed following H_2O_2 activation. Atomically disperse Ti atoms, on surfaces of amorphous silicas[8,79−81] and within zeolites (e.g., TS-1[33,80,82,83] and Ti-BEA[8,22,43,84,85]), activate H_2O_2 to form pools of titanium-hydroperoxo (Ti−OOH) and peroxo (Ti-(η^2-O_2)) intermediates. The ligand-to-metal charge-transfer (LMCT) energies of such species reflect the tendency of these intermediates to exchange electron density with the active site and, therefore, provide one quantitative measure of the electronic structure of these reactive surface species. Figure 5

DOI: 10.1021/jacs.8b12861
J. Am. Chem. Soc. XXXX, XXX, XXX−XXX

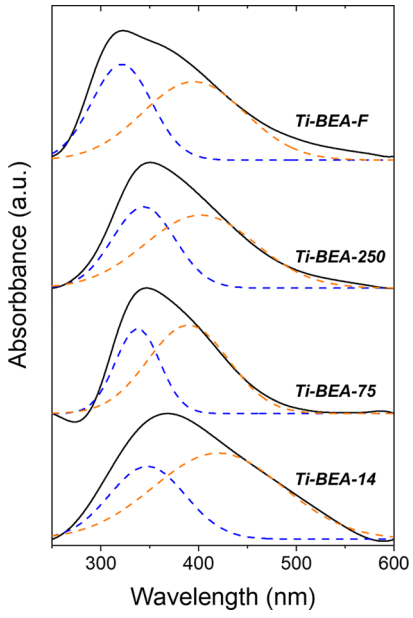

Figure 5. UV−vis spectra of Ti-(η^2-O_2)- (blue) and Ti−OOH- (orange) saturated surfaces of Ti-BEA-14, Ti-BEA-75, Ti-BEA-250, and Ti-BEA-F obtained in situ (0.01 M H_2O_2 in CH_3CN, 313 K). Dashed curves represent Gaussian fits to UV−vis absorbance features. The background for each spectrum was obtained in flowing CH_3CN at 313 K. Spectra are normalized by their maximum absorbance and vertically offset for clarity.

shows steady-state UV−vis spectra of Ti-BEA-14, Ti-BEA-75, Ti-BEA-250, and Ti-BEA-F (0.01 M H_2O_2, 0.04 M H_2O, in CH_3CN, 313 K), and the corresponding UV−vis spectra for all Ti-BEA are shown in Figure S13. All UV−vis spectra reveal complex absorbance features between 280 and 550 nm, consistent with reports for Ti−OOH and Ti-(η^2-O_2) species on Ti atoms grafted to mesoporous silicas[8,79−81] and within the framework of MFI[80,82,86] or BEA zeolites.[8,42,43] Spectral deconvolution of these UV−vis features reveals two distinct bands at ∼310 and ∼410 nm, which correspond to Ti-(η^2-O_2) and Ti−OOH, respectively.[8,79,80] Table 2 and Figure S13b show that LMCT energies for neither Ti-(η^2-O_2) nor Ti−OOH depend on [$(SiOH)_4$], which strongly suggests that the proximity and density of $(SiOH)_4$ have a negligible impact on the electronic properties of the active intermediates for alkene epoxidation on Ti-BEA.

The identity of the reactive intermediate was probed by examining the stereospecificity for the epoxidation of *Z*-stilbene over all Ti-BEA (1 mM *Z*-stilbene, 0.01 M H_2O_2 in CH_3CN, 313 K). Hydroperoxide species (i.e., M-OOH) epoxidize C=C through a "butterfly" transition state that results in a concerted O-atom transfer and retains the stereochemistry of the alkene.[87−89] Alternatively, peroxo complexes (i.e., Ti-(η^2-O_2)) may react through a stepwise mechanism that allows for C−C bond rotation and different stereochemistry for the product.[90,91] Table 2 shows that epoxidation of *Z*-stilbene over Ti-BEA-X predominantly produces *Z*-stilbene oxide in all cases, which suggests that Ti−OOH is the active species for epoxidation and does not vary significantly with [$(SiOH)_4$]. These observations agree with the general consensus that Ti−OOH species are responsible for epoxidation reactions on TS-1,[33,87,92,93] Ti-SiO_2,[63,80,94,95] and Ti-BEA materials.[8,43,84]

These analyses show that variations in [$(SiOH)_4$] do not cause detectable changes in the identity or LMCT energies of the Ti−OOH species that participate in epoxidations of alkenes. Such conclusions are also consistent with the quantitative similarities in $\Delta H_{CD_3CN,Ti}$ (see above), which show that the electronic exchange between adsorbates and framework Ti atoms does not vary over the range of [$(SiOH)_4$] studied here. Collectively, these results suggest that any catalytic consequences related to changes in the value of [$(SiOH)_4$] are not likely caused by simple differences in charge transfer among only reactive species and framework Ti atoms.

3.4. Reaction Pathways for Epoxidation and H_2O_2 Decomposition over Ti-BEA Catalysts. Turnover rates for epoxidation[8,42,43] and sulfoxidation[85] reactions depend on the concentrations of the organic substrate, the oxidant (H_2O_2), and the reaction products (e.g., epoxides and sulfoxides) because these concentrations determine the coverage of reactive surface species at Ti atoms and the availability of

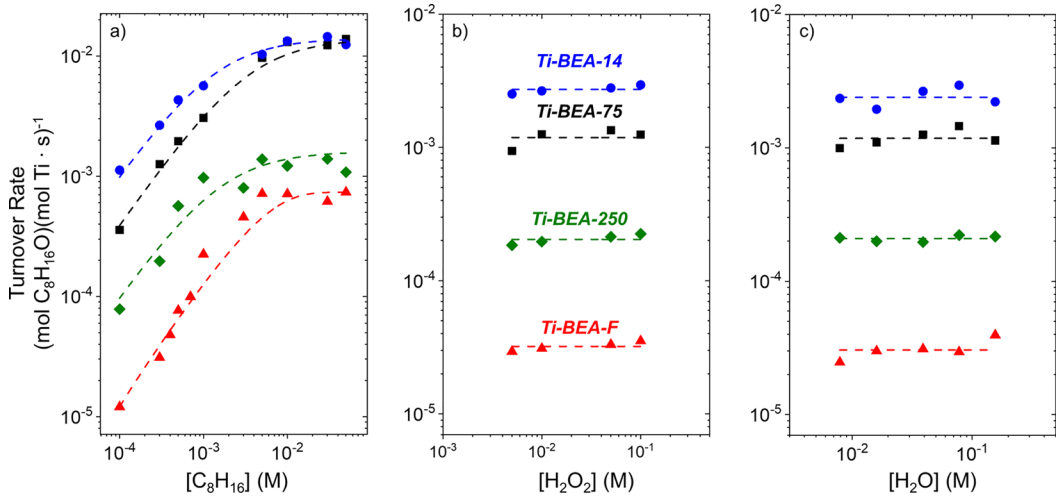

Figure 6. Turnover rates for the formation of $C_8H_{16}O$ as a function of (a) [C_8H_{16}] (0.01 M H_2O_2, 0.039 M H_2O), (b) [H_2O_2] (3×10^{-4} M C_8H_{16}), and (c) [H_2O] (3×10^{-4} M C_8H_{16}, 0.01 M H_2O_2) on Ti-BEA-14 (blue ●), Ti-BEA-75 (■), Ti-BEA-250 (green ◆), and Ti-BEA-F (red ▲) in CH_3CN at 313 K. Dashed lines represent fits to eqs 8 (Figure 6a) and 9 (Figure 6b,c).

DOI: 10.1021/jacs.8b12861
J. Am. Chem. Soc. XXXX, XXX, XXX−XXX

Scheme 1. Proposed Elementary Steps for C_8H_{16} Epoxidation and H_2O_2 Decomposition over Ti-BEA[a]

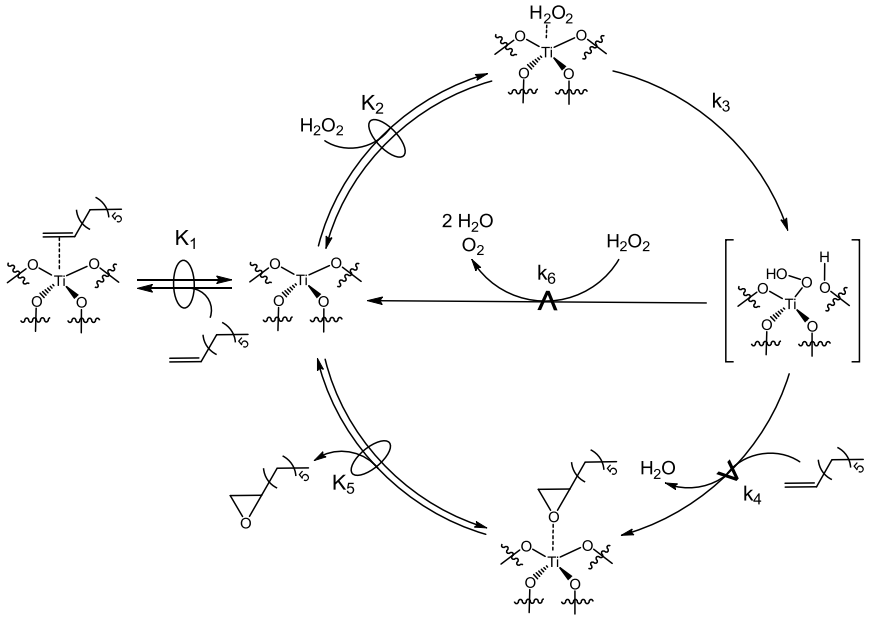

[a]Symbol ⇌ represents a quasi-equilibrated step, whereas → represents a kinetically relevant step. The Ti−OOH intermediates drawn are intended to represent the pool of Ti−OOH and Ti-(η^2-O_2) species that is present, as shown by UV−vis (Figure 5).

coreactants. Figure 6 shows that all Ti-BEA give turnover rates for 1-octene epoxidation that exhibit nearly indistinguishable dependencies on the concentrations of 1-octene (C_8H_{16}) (Figure 6a), H_2O_2 (Figure 6b), or H_2O (Figure 6c) despite significant differences in the [$(SiOH)_4$] and in the turnover rates. Notably, Ti-BEA-14 (the material with the greatest density of silanol nests) gives epoxidation turnover rates that are two orders of magnitude greater than those for Ti-BEA-F (the sample with the fewest silanol groups), which indicates that the presence of $(SiOH)_4$ results in a significant increase in epoxidation rates under these conditions. Specifically, turnover rates for 1-octene in Ti-BEA materials increase monotonically with the density of $(SiOH)_4$ groups across the seven Ti-BEA structures (Figure 7a), for reasons described below. For clarity, turnover rates as a function of reactant and coproduct concentrations for materials with intermediate densities of $(SiOH)_4$ groups (i.e., Ti-BEA-12.5, -20, and -150) are shown only in Figure S14a−c.

All Ti-BEA exhibit two regimes that differ in how turnover rates depend on the concentrations of reactants. At low $[C_8H_{16}]/[H_2O_2]$ ($\ll$0.5), rates increase linearly with $[C_8H_{16}]$ and remain constant for different $[H_2O_2]$, which suggests that reactive intermediates derived from H_2O_2 (i.e., Ti−OOH) cover a majority of active sites. At greater values of $[C_8H_{16}]/[H_2O_2]$ ($\gg$0.5), turnover rates do not depend on $[C_8H_{16}]$, which indicates that C_8H_{16}-derived intermediates saturate active sites. Notably, rates remain constant with changes in $[H_2O]$ (4−160 mM), presumably because the quantities of H_2O in the pores of each BEA structure remain nearly constant within this range of $[H_2O]$. The dependence of $C_8H_{16}O$ formation on reactant and coproduct (i.e., H_2O) concentrations agree closely with prior findings for group 4 and 5 metal atoms substituted into zeolite *BEA for the epoxidation of cyclohexene[42,43] and styrene,[8] and the sulfoxidation of 2,5-dimethylthiophene.[85]

Scheme 1 depicts a series of elementary steps that describe the measured effects of $[C_8H_{16}]$, $[H_2O_2]$, and $[H_2O]$ on the rates of $C_8H_{16}O$ formation. This catalytic cycle involves the quasi-equilibrated adsorption of C_8H_{16} (step 1) and H_2O_2 (step 2) and the irreversible activation of adsorbed H_2O_2 (step 3) to form a pool of intermediates. Within this pool of species, Ti−OOH (Section 3.3) reacts with proximate C_8H_{16} (step 4) or H_2O_2 (step 6) molecules within kinetically relevant processes to form $C_8H_{16}O$ or decomposition products (e.g., O_2 and H_2O), respectively. Molecules of $C_8H_{16}O$ desorb in a quasi-equilibrated manner (step 5) after their formation.[8,42,43] Following Scheme 1, rates for $C_8H_{10}O$ formation (r_E) take the form

$$r_E = k_4[C_8H_{16}][\text{Ti}-\text{OOH}] \tag{7}$$

where [Ti−OOH] is the number of Ti−OOH intermediates and k_i is the rate constant for step i in Scheme 1. The application of the pseudo-steady-state hypothesis to the number of Ti−OOH and a site balance over all possible states of the Ti active site allows eq 7 to be restated as

$$\frac{r_E}{[L]} = \frac{\frac{k_3k_4K_2[C_8H_{16}][H_2O_2]}{k_4[C_8H_{16}]+k_6[H_2O_2]}}{1 + K_1[C_8H_{16}] + K_2[H_2O_2] + \frac{k_3K_2[H_2O_2]}{k_4[C_8H_{16}]+k_6[H_2O_2]} + \frac{[C_8H_{16}O]}{K_5}} \tag{8}$$

where [L] is the total number of active sites and K_i is the equilibrium constant for step i. The five terms in the denominator correspond to active metal atoms occupied by CH_3CN (i.e., the solvent), C_8H_{16}, H_2O_2, Ti−OOH, or $C_8H_{16}O$, respectively. The derivation of the analogous rate expression for H_2O_2 decomposition is shown in Section S4.2.

Reaction conditions that give turnover rates that are proportional to $[C_8H_{16}]$ and invariant with changes in $[H_2O_2]$ result in surfaces saturated with pools containing reactive Ti−OOH intermediates,[8,42,43,85] which reduces eq 8 to the form

$$\frac{r_E}{[L]} = k_4[C_8H_{16}] \tag{9}$$

DOI: 10.1021/jacs.8b12861
J. Am. Chem. Soc. XXXX, XXX, XXX−XXX

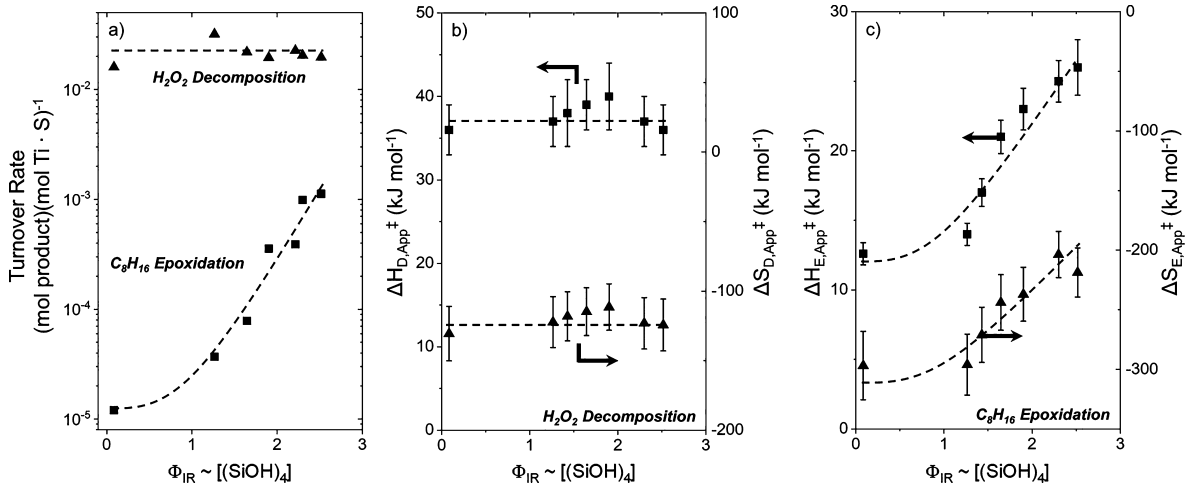

Figure 7. (a) Turnover rates for C_8H_{16} epoxidation (■) and H_2O_2 decomposition (▲) (0.1 mM C_8H_{16}, 0.01 M H_2O_2, 0.039 M H_2O, 313 K). Apparent activation enthalpies (■) and entropies (▲) for (b) H_2O_2 decomposition and (c) C_8H_{16} epoxidation (0.1 mM C_8H_{16}, 0.01 M H_2O_2, 0.039 M H_2O) as functions of Φ_{IR} (i.e., a measure of [(SiOH)$_4$]; Section 3.1). Dashed curves are intended to guide the eye. Polanyi plots used to determine $\Delta H_{App}^{\ddagger}$ and $\Delta S_{App}^{\ddagger}$ are shown in Figure S15.

The form of eq 9 reproduces the observed dependencies of turnover rates on $[C_8H_{16}]$, $[H_2O_2]$, and $[H_2O]$ from Figure 6a–c, under those conditions where $[H_2O_2]$ is greater than $[C_8H_{16}]$. When values of $[C_8H_{16}]$ significantly exceed those for $[H_2O_2]$, the full rate expression (eq 8) only reproduces the observed dependence on $[C_8H_{16}]$ under two limiting conditions. In one instance, eq 8 matches these data when adsorbed $C_8H_{16}O$ is the most abundant reactive intermediate (MARI) and the rate of epoxidation is far greater than H_2O_2 decomposition (i.e., $k_4[C_8H_{16}] > k_6[H_2O_2]$), which agrees with results from the epoxidation of cyclohexene[43] and styrene[8] and the sulfoxidation of 2,5-dimethylthiophene[85] on Ti-BEA. Then, eq 8 reduces to yield

$$\frac{r_E}{[L]} = \frac{k_3K_2K_5[H_2O_2]}{[C_8H_{16}O]} \quad (10)$$

which describes epoxidation rates that do not depend on $[C_8H_{16}]$ (Figure 6a). This series of assumptions holds for hydrophilic Ti-BEA-X (X = 12.5, 14, 20, and 75), where rates of epoxidation are greater than rates of H_2O_2 decomposition at high $[C_8H_{16}]/[H_2O_2]$. Yet these conditions are not met for hydrophobic Ti-BEA-X (X = 150, 250, and F) samples, because rates for H_2O_2 decomposition are greater than those for epoxidation (i.e., $k_6[H_2O_2] > k_4[C_8H_{16}]$). Under these conditions, the general rate expression recreates measured concentration dependencies when Ti active sites become saturated with C_8H_{16}, which simplifies eq 8 to

$$\frac{r_E}{[L]} = \frac{k_3k_4K_2}{k_6K_1} \quad (11)$$

Equation 11 is consistent with the measured dependence of epoxidation rates on $[C_8H_{16}]$ (Figure 6a). Equitable comparisons of turnover rates and apparent activation barriers across this series of Ti-BEA catalysts can only be made under reaction conditions that result in equivalent surface coverages of surface species (i.e., all Ti-BEA saturated with Ti–OOH) and equal concentrations of liquid-phase reagents. The next section describes a series of such measurements and the associated interpretations that reveal the molecular interactions responsible for a 100-fold increase in epoxidation turnover rates and selectivities introduced by increasing the density of $(SiOH)_4$ groups.

3.5. Effects of Hydrogen-Bonding Interactions with Silanol Groups on Turnover Rates and Excess Free Energies of Activation. Turnover rates for C_8H_{16} epoxidation increase by a factor of 100 between the most hydrophobic and hydrophilic Ti-BEA. H_2O_2 decomposition rates, however, remain constant, with differences in $[(SiOH)_4]$ for this series of Ti-BEA (Figure 7a; 0.1 mM C_8H_{16}, 10 mM H_2O_2, 39 mM H_2O, 313 K). These differences lead to significantly greater epoxidation turnover rates and H_2O_2 selectivities on Ti-BEA with greater $[(SiOH)_4]$, where selectivity is defined here as the ratio of the rate of epoxide formation to that of H_2O_2 consumption. These large changes in epoxidation turnover rates do not reflect differences in intraporous H_2O_2 or C_8H_{16} concentrations[21,24,37] because turnover rates do not depend on $[H_2O_2]$ under these conditions, and the measured uptake of C_8H_{16} is identical among all Ti-BEA (0.1 mM C_8H_{16}, 0.039 M H_2O, 313 K; Figure S16). Moreover, the significant differences in epoxidation turnover rates and selectivities do not arise from differences in the electronic properties of the active site (Section 3.2) or active intermediates (Section 3.3), nor are they due to differences in the mechanism for epoxidation (Section 3.4), as all of these factors are indistinguishable among the Ti-BEA catalysts within this study.

Figure 7b shows that apparent activation enthalpies and entropies for H_2O_2 decomposition ($\Delta H_{D,App}^{\ddagger}$ and $\Delta S_{D,App}^{\ddagger}$) do not vary with $[(SiOH)_4]$ when measured at identical coverages of reactive species (i.e., Ti–OOH MARI), which suggests that the transition state for H_2O_2 decomposition is not sensitive to the proximity and density of $(SiOH)_4$. In contrast, Figure 7c indicates that apparent activation enthalpies and entropies for C_8H_{16} epoxidation ($\Delta H_{E,App}^{\ddagger}$ and $\Delta S_{E,App}^{\ddagger}$) vary between the most hydrophobic and hydrophilic Ti-BEA by 12 kJ mol^{-1} and 93 J mol^{-1} K^{-1}, respectively. These differences in the values for $\Delta H_{E,App}^{\ddagger}$ and $\Delta S_{E,App}^{\ddagger}$ account for the 100-fold increase in turnover rates across these materials. Notably, comparisons of these $\Delta H_{App}^{\ddagger}$ and $\Delta S_{App}^{\ddagger}$ values between the two reaction pathways strongly suggest that differences in the stability of transition states for epoxidation (and not the stability of the

DOI: 10.1021/jacs.8b12861
J. Am. Chem. Soc. XXXX, XXX, XXX–XXX

Ti−OOH surface species) are primarily responsible for the catalytic differences among Ti-BEA caused by the presence of $(SiOH)_4$ groups.

Transition-state theory postulates that reaction rates reflect the stability of an activated complex (i.e., a transition state) relative to a known reference state (i.e., Ti−OOH and fluid-phase C_8H_{16} or H_2O_2) within the catalytic cycle (Scheme 2).

Scheme 2. Proposed Sequence of Steps for the Formation of the Transition State for Epoxidation (Step 2.1) or Decomposition of H_2O_2 (Step 2.2)

$$Ti-(OOH)+C_8H_{16} \overset{K_E^{\ddagger}}{\rightleftharpoons} Ti-(OOH)-C_8H_{16}^{\ddagger} \quad (2.1)$$

$$Ti-(OOH)+H_2O_2 \overset{K_D^{\ddagger}}{\rightleftharpoons} Ti-(OOH)-H_2O_2^{\ddagger} \quad (2.2)$$

Here Ti−OOH−$C_8H_{16}^{\ddagger}$ and Ti−OOH−$H_2O_2^{\ddagger}$ are the transition states for C_8H_{16} epoxidation and H_2O_2 decomposition, respectively, and $K_x^{\ddagger}$ is the corresponding transition-state equilibrium constant for epoxidation ($K_E^{\ddagger}$) or H_2O_2 decomposition ($K_D^{\ddagger}$).

These catalytic reactions occur at solid−liquid interfaces that introduce specific molecular interactions (e.g., hydrogen bonds) that introduce thermodynamic nonidealities and require rates to be described as functions of reactant activities and activity coefficients.[96] Within this conceptual framework, and with Ti−OOH as the MARI, rates of epoxidation (r_E) and H_2O_2 decomposition (r_D) equal

$$r_E = \frac{k_B T}{h} e^{(-\Delta G_E^{0,\ddagger}/RT)} \frac{a_{Ti-OOH}}{\gamma_{\ddagger,E}} a_{C_8H_{16}} \quad (12a)$$

$$r_D = \frac{k_B T}{h} e^{(-\Delta G_D^{0,\ddagger}/RT)} \frac{a_{Ti-OOH}}{\gamma_{\ddagger,D}} a_{H_2O_2} \quad (12b)$$

Within each equation, $\Delta G^{0,\ddagger}$ is the Gibbs free energy of activation at the standard state, a_j is the thermodynamic activity of species j, and $\gamma_{\ddagger}$ is the activity coefficient for the relevant transition-state complex. For the comparisons made here, the standard state is defined as one that contains negligible hydrogen-bond donors present at the solid−liquid interface, which is best represented by the pore environment of hydrophobic Ti-BEA-F. The activity coefficients of Ti−OOH, C_8H_{16}, and H_2O_2 will depend on hydrogen-bonding interactions, which can be described as a function of the excess Gibbs free-energy (G_j^{ε}) contribution

$$\gamma_j = e^{(G_j^{\varepsilon}/RT)} \quad (13)$$

By combining free-energy terms, eq 12a is then restated as

$$\frac{r_E}{[L]} = \frac{k_B T}{h} e^{(-\Delta G_{E,App}^{\ddagger}/RT)} [C_8H_{16}] \quad (14a)$$

$$\frac{r_D}{[L]} = \frac{k_B T}{h} e^{(-\Delta G_{D,App}^{\ddagger}/RT)} [H_2O_2] \quad (14b)$$

which also recognizes that the number of Ti−OOH intermediates ([Ti−OOH]) equals that of the active sites ([L]) under the conditions used to measure $\Delta H_{App}^{\ddagger}$ and $\Delta S_{App}^{\ddagger}$ values.

The apparent free energies of activation ($\Delta G_{App}^{\ddagger}$) are given by

$$\Delta G_{E,App}^{\ddagger} = (G_E^{0,\ddagger} + G_E^{\varepsilon,\ddagger}) - (G_{Ti-OOH}^{0} + G_{Ti-OOH}^{\varepsilon}) - (G_{C_8H_{16}}^{0} + G_{C_8H_{16}}^{\varepsilon}) \quad (15a)$$

$$\Delta G_{D,App}^{\ddagger} = (G_D^{0,\ddagger} + G_D^{\varepsilon,\ddagger}) - (G_{Ti-OOH}^{0} + G_{Ti-OOH}^{\varepsilon}) - (G_{H_2O_2}^{0} + G_{H_2O_2}^{\varepsilon}) \quad (15b)$$

where $G^{\ddagger}$, G_{Ti-OOH}, and G_j are the free energies of the transition state, Ti−OOH, and fluid-phase coreactants, respectively. The excess free-energy terms of the fluid-phase coreactants (i.e., $G_{C_8H_{16}}^{\varepsilon}$ and $G_{H_2O_2}^{\varepsilon}$) do not vary with $[(SiOH)_4]$ because these species are not contained within the pores of Ti-BEA. Consequently, differences in the apparent activation free energies ($\Delta\Delta G^{\ddagger}$) between a given Ti-BEA and Ti-BEA-F reflect changes only in the excess properties of the relevant transition states and Ti−OOH

$$\Delta\Delta G_E^{\ddagger} = G_E^{\varepsilon,\ddagger} - G_{Ti-OOH}^{\varepsilon} \quad (16a)$$

$$\Delta\Delta G_D^{\ddagger} = G_D^{\varepsilon,\ddagger} - G_{Ti-OOH}^{\varepsilon} \quad (16b)$$

Activation parameters for H_2O_2 decomposition do not vary with $[(SiOH)_4]$ ($\Delta H_{D,App}^{\ddagger}$ = 37 ± 8 kJ mol^{-1}; $\Delta S_{D,App}^{\ddagger}$ = −120 ± 45 J mol^{-1} K^{-1}), which indicates that $G_D^{\varepsilon,\ddagger}$ and G_{Ti-OOH}^{ε} are either serendipitously equal or that the free energies of these complexes do not depend on the $[(SiOH)_4]$ within these materials (i.e., $G_D^{\varepsilon,\ddagger}$ and G_{Ti-OOH}^{ε} equal zero). The invariance in these values may be explained in two ways. First, Ti−OOH and the transition states for H_2O_2 decomposition may nucleate small clusters of H_2O, as both species are capable of donating and accepting hydrogen bonds. The formation of H_2O clusters at Ti−OOH and H_2O_2 decomposition transition states diminishes the effects of nearby H_2O clusters that form at proximate $(SiOH)_4$.[97,98] Second, the effective diameter of Ti−OOH and the transition state for H_2O_2 decomposition may be too small to interact with the pore walls of BEA[8] and thus may be insensitive to nearby $(SiOH)_4$ and H_2O clusters stabilized at these sites. In the context of either explanation, the strong dependence of turnover rates for C_8H_{16} epoxidation on the number of proximate $(SiOH)_4$ groups must arise from differences in the excess free energies of transition states for epoxidation (i.e., $G_E^{\varepsilon,\ddagger}$).

Values of $G_E^{\varepsilon,\ddagger}$ and, by extension, $H_E^{\varepsilon,\ddagger}$ and $S_E^{\varepsilon,\ddagger}$ that recognize differences in the density of $(SiOH)_4$ groups seem likely to do so via interactions of the aliphatic tail of this transition state with the local environment. Values of $\Delta H_{E,App}^{\ddagger}$ are lowest in Ti-BEA-F because the aliphatic tail of the transition state interacts weakly with siloxane pore walls through dispersive forces. The pores of Ti-BEA-F should contain acetonitrile and negligible concentrations of water molecules, primarily in loosely bound, disordered states. Consequently, the values of $\Delta S_{E,App}^{\ddagger}$, which are most negative for Ti-BEA-F among all Ti-BEA, predominantly reflect the loss of entropy related to the coordination of 1-octene to Ti−OOH and changes in the structure of solvating acetonitrile. However, hydrogen-bonded clusters of water molecules near active sites within hydrophilic Ti-BEA materials (e.g., Ti-BEA-14) interact unfavorably with the alkyl chain of epoxidation transition states, which appear as greater values of $\Delta H_{E,App}^{\ddagger}$ (from 12 kJ mol^{-1} for Ti-BEA-F to 25 kJ mol^{-1} for Ti-BEA-14) as a result of increasing the $H_E^{\varepsilon,\ddagger}$. The disruption of these hydrogen-bonded water clusters manifests as large positive $S_E^{\varepsilon,\ddagger}$ values

DOI: 10.1021/jacs.8b12861
J. Am. Chem. Soc. XXXX, XXX, XXX−XXX

that reflect the reorganization of these confined water clusters to accommodate the epoxidation transition states. Ultimately, differences among activation free energies for epoxidation ($\Delta\Delta G_{E,App}^{\ddagger}$) are dominated by entropic contributions under these conditions, which agrees with the expectations that such changes are exacerbated within confining environments that can lead to significant reorganization of molecules.[99−101]

Values of $H_E^{\varepsilon,\ddagger}$ and $S_E^{\varepsilon,\ddagger}$ that increase with $[(SiOH)_4]$ in Ti-BEA (Figure 7b,c) are semiquantitatively consistent with the expected enthalpic costs and entropic benefits of disrupting hydrogen-bonded water clusters, in this case, by the formation of the transition states. The rupture of a single hydrogen bond among water molecules at the interface between bulk liquid water and a nonpolar solute increases the enthalpy of the system by ∼10 kJ mol^{-1} and simultaneously increases the entropy by 25 J mol^{-1} K.[102,103] Water confined within nanometer-scale voids (e.g., in a zeolite) possesses significantly lower entropies than bulk H_2O as a result of structuring and highly correlated molecular motion within pores <1 nm in diameter.[100,101] Thus the interaction of transition states for epoxidation with H_2O clusters in these confined spaces results in an entropic gain much larger than anticipated from comparisons to bulk liquid water. The changes in $G_E^{\varepsilon,\ddagger}$ do not, however, correspond entirely to restructuring of confined H_2O clusters because the value of $G_E^{\varepsilon,\ddagger}$ reflects the net change in free energy that results from interactions among silanol nests, the H_2O clusters stabilized at these nests, the surrounding CH_3CN solvent molecules, and the epoxidation transition states. Deconvolution of these effects requires detailed kinetic and calorimetric measurements obtained over a range of conditions, which are in progress. Despite the difficulties in deconvoluting the contributions of each set of molecular interactions, these changes in $G_E^{\varepsilon,\ddagger}$ can be attributed to water-mediated hydrogen-bond donation and acceptance among the species present about the active site. In the following section, we demonstrate that the hydrogen bonds between silanol nests, H_2O clusters, and transition states within the pores of Ti-BEA catalysts increase alkene epoxidation rates regardless of the identity of the oxidant by comparing rates obtained under hydrous and anhydrous conditions.

3.6. Differences in Epoxidation Rates of Ti-BEA Caused by Hydrogen Bonding among Reactants, Surfaces, and Solvents. Figure 8 shows that turnover rates for C_8H_{16} epoxidation with aqueous H_2O_2 (0.1 mM C_8H_{16}, 39 mM H_2O, 10 mM H_2O_2) increase by a factor of 100 as the density of silanol groups increases from ∼0 to 5 (unit cell)$^{-1}$ between the most hydrophobic and hydrophilic Ti-BEA. In contrast, epoxidation turnover rates using *tert*-butyl hydroperoxide (*t*-BuOOH) under anhydrous conditions (0.1 mM C_8H_{16}, 10 mM *t*-BuOOH, 313 K) give turnover rates that differ by less than a factor of 2. Under anhydrous reaction conditions, $(SiOH)_4$ groups cannot readily influence the stability of transition states for epoxidation due to the lack of water clusters to facilitate these interactions. Yet the turnover rates for C_8H_{16} epoxidation with *t*-BuOOH increase by a factor of 20 when the density of $(SiOH)_4$ is increased from ∼0 to 5 (unit cell)$^{-1}$ in the presence of small amounts of H_2O (39 mM H_2O). Presumably, these small concentrations of H_2O introduce similar differences in $G_E^{\varepsilon,\ddagger}$ across the series of Ti-BEA, as observed in epoxidations with aqueous H_2O_2 (Section 3.5). Turnover rates for epoxidation within Ti-BEA-F are largely unaffected by the addition of H_2O to the solvent, which

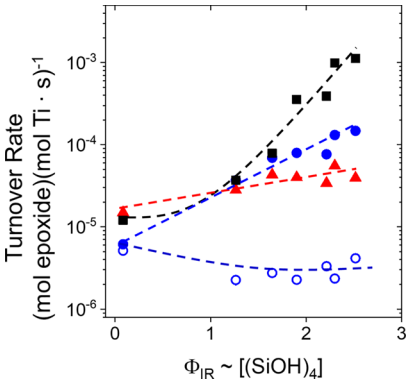

Figure 8. Turnover rates for C_8H_{16} epoxidation (■; 0.1 mM C_8H_{16}, 0.01 M H_2O_2, 0.039 M H_2O, 313 K), C_8H_{16} epoxidation with *t*-BuOOH (0.1 mM C_8H_{16}, 0.01 M *t*-BuOOH, 313 K) under anhydrous conditions (blue ○) and with 0.039 M H_2O (blue ●), and $C_6H_{11}OH$ epoxidation (red ▲; 0.1 mM $C_6H_{11}OH$, 0.01 M H_2O_2, 0.039 M H_2O, 313 K) over Ti-BEA as a function of Φ_{IR} (i.e., a measure of $[(SiOH)_4]$. Dashed curves are intended to guide the eye.

is consistent with the expectation that extended H_2O clusters cannot form within pores of Ti-BEA-F under these conditions.[28,29] These observations and interpretations further support the conclusion that the presence of structured H_2O clusters within pores leads to large changes in $G_E^{\varepsilon,\ddagger}$ within the most hydrophilic Ti-BEA that reflect the complex network of hydrogen bonds formed between the transition states for epoxidation, nearby H_2O clusters, and $(SiOH)_4$ groups.

The chemical functionality of the reactant should also influence the dependence of $G_E^{\varepsilon,\ddagger}$ on $[(SiOH)_4]$, particularly if the transition state for epoxidation can donate or accept hydrogen bonds. Figure 8 shows that turnover rates for 5-hexene-1-ol ($C_6H_{11}OH$) epoxidation increase with silanol density by only a factor of 5 across this series of catalysts, which is much less than the 100-fold difference for epoxidation of C_8H_{16} across the same materials. The transition state for $C_6H_{11}OH$ epoxidation includes a terminal −OH, which is less likely to perturb the structure of proximate H_2O clusters than C_8H_{16}. The comparison between the change in epoxidation rates for these two substrates (i.e., $C_6H_{11}OH$ and C_8H_{16}) is consistent with rates that increase due to disruptive interactions between the epoxidation transition states and H_2O clusters and the associated entropy gains.

3.7. Implications of Relative Hydrophilicity within Zeolite Catalysis. Collectively, these data show that the changes in the density of $(SiOH)_4$ can greatly influence the rates of a given reaction in the presence of H_2O. The analysis presented here, which describes how the excess free energies of the transition state for a given reaction may change with $[(SiOH)_4]$, is extended to other catalytic chemistries within zeolites to yield new interpretations for the effects of hydrophobicity in liquid-phase catalysis.

Rates of Baeyer−Villiger (BV) oxidations are greater for Sn-BEA catalysts synthesized by postsynthetic modification relative to defect-free materials (i.e., synthesized in fluoride media), such that oxidation rates of cyclohexanone with aqueous H_2O_2 (0.33 M cyclohexanone, 0.5 M H_2O_2, 1.8 M H_2O, 353 K)[27] and for 2-adamantanone with anhydrous *t*-BuOOH (2 M ketone, 4 M *t*-BuOOH, 363 K),[104] differ by factors of 6 and 3, respectively, between postsynthetically modified Sn-BEA and defect-free Sn-BEA. The original authors proposed that silanol groups increase BV oxidation rates by

DOI: 10.1021/jacs.8b12861
J. Am. Chem. Soc. XXXX, XXX, XXX−XXX

facilitating the coordination of cyclohexanone to the Sn active sites.[27] Differences in the rates of 2-adamantanone oxidation, on the contrary, were attributed to diffusion limitations within pores of defect-free Sn-BEA that reduced the availability of reactants at Sn active sites.[104] The observations in these publications are consistent with the manner by which rates should change as a result of $G^{\varepsilon,\ddagger}$ for BV oxidation (i.e., the Criegee adduct)[105] that decreases due to disruption of the confined H_2O or ROH clusters stabilized at nearby $(SiOH)_4$.

Meerwin–Ponndorf–Verley (MPV) reduction rates are greater in defect-free Zr-BEA (synthesized in fluoride media) relative to those synthesized by postsynthetic incorporation of Zr atoms. Specifically, MPV rates were 1.5 times higher in the hydrophobic Zr-BEA (522 versus 350 h^{-1}, 1 M 4-*tert*-butylcyclohexanone in 2-propanol, 355 K).[106] The authors do not discuss the origins of these differences within their manuscript.[106] These MPV reactions were conducted under ostensibly anhydrous conditions, such that ROH clusters, rather than H_2O, are likely formed through hydrogen-bonding interactions with $(SiOH)_4$. On the basis of our analysis, values of $G^{\varepsilon,\ddagger}$ for MPV reduction (i.e., the intermolecular hydride transfer between 2-propanol and ketone bound to the same Zr site)[107] may increase with $(SiOH)_4$, because the bulky *tert*-butyl moieties of the ketone interact with the defect-free pore walls and are enthalpically stabilized (i.e., lower $H^{\varepsilon,\ddagger}$). Clusters of 2-propanol clusters that form at nearby $(SiOH)_4$ are not stabilized by hydrogen bonds to the same extent as H_2O; consequently, these clusters do not provide large entropy gains when they accommodate transition states. Collectively, the $G^{\varepsilon,\ddagger}$ for MPV reduction is dictated by the changes in the excess enthalpies that arise from interactions of the hydrophobic ketone with the pore walls of Zr-BEA.

The interpretation of the influence of hydrogen-bonding interactions among SiOH, H_2O, and alkene epoxidation transition states seems to also be consistent with reported comparisons among cyclohexene and 1-hexene.[24,35] epoxidation rates on Ti-containing zeolite catalysts. For example, the rates of cyclohexene epoxidation with aqueous H_2O_2 are 50% greater on Ti-MWW catalysts synthesized by postsynthetic modification than on defect-free [Ti,B]-MWW (27 h^{-1} versus 18 h^{-1}; 5 M cyclohexene, 1 M H_2O_2, 3.9 M H_2O, 333 K).[108] Here the authors proposed that differences in epoxidation rates result from decreases in the zeolite framework electronegativity that arise from Lewis acidic B atoms. Similarly, epoxidation rates of 1-hexene are 65–125% greater on hydrophilic TS-1 as compared with conventional hydrophobic TS-1 (1 M 1-hexene, 1 M H_2O_2, 3.9 M H_2O, 333 K).[24,35] The authors in one study proposed that the increased rates reflected a greater concentration of H_2O_2 near active sites caused by favorable interactions with SiOH groups. Alternatively, in the other study, the large differences in epoxidation rates were attributed to differences in the electronic properties of the Ti active sites.[35] It seems more likely, however, that the presence of H_2O stabilized at SiOH within the Ti-zeolite catalysts in these studies results in large increases in the excess entropy of the epoxidation transition states (i.e., $S^{\varepsilon,\ddagger}$) due to the disruption of these confined H_2O clusters within the hydrophilic zeolite pores.

These studies represent only a portion of an extensive body of literature that seeks to explain differences in rates and selectivities among materials with varying hydrophilicity, which often can be thought of as differences in densities of various silanol features. Collectively, the analysis and interpretation of results (within this work and those cited above) show that the excess free energies of the transition states for a given reaction pathway depend strongly on the presence, density, and proximity of extended hydrogen-bonded networks within zeolite catalysts. These complex interactions encompass the formation and restructuring of these intraporous solvent networks, which depend intimately on the chemical functionality of the reactants.

4. CONCLUSIONS

Epoxidation of alkenes by H_2O_2 and H_2O_2 decomposition reactions occurs at framework Ti atoms within Ti-BEA catalysts, and turnover rates for epoxidation strongly depend on the presence, density, and proximity of the epoxidation transition states to $(SiOH)_4$ moieties. Turnover rates for 1-octene epoxidation increase monotonically with the density of $(SiOH)_4$ in Ti-BEA, where materials containing ~5 $(SiOH)_4$ (unit cell)$^{-1}$ possess rates that are 100 times greater than Ti-BEA that are nearly defect-free. Rates of H_2O_2 decomposition, however, are insensitive to $[(SiOH)_4]$ across the Ti-BEA tested here. These differences in epoxidation catalysis do not reflect variations in the electron affinity of the Ti active sites among the series of Ti-BEA because neither measured adsorption enthalpies for CD_3CN to Ti atoms nor ligand-to-metal charge-transfer energies for Ti–OOH and Ti-(η^2-O_2) species differ with the density of $(SiOH)_4$. Mechanistic interpretations of epoxidation rates measured as a function of reactant concentrations, in combination with in situ UV–vis measurements and radical-clock reactions with *cis*-stilbene, show that the mechanism for epoxidation and the identity and electronic properties of reactive Ti–OOH intermediates do not vary with $(SiOH)_4$ density.

Apparent free energies of activation for 1-octene epoxidation decrease with increasing densities of $(SiOH)_4$ within reactant solutions that contain small concentrations of water (39 mM), which indicates that water molecules and their hydrogen-bonding interactions help stabilize epoxidation transition states. Specifically, apparent activation enthalpies and entropies for 1-octene epoxidation are 13 kJ mol^{-1} lower and 93 J mol^{-1} K^{-1} more negative on defect-free Ti-BEA than Ti-BEA containing ~5 $(SiOH)_4$ (unit cell)$^{-1}$, respectively. Yet these same quantities for the decomposition of H_2O_2 remain constant, within the uncertainty of the measurements for all Ti-BEA. These comparisons show that smaller apparent entropy losses for forming epoxidation transition states in Ti-BEA with the most $(SiOH)_4$ are responsible for the significantly greater epoxidation turnover rates and selectivities in these materials.

The differences in apparent activation enthalpies and entropies with the density of $(SiOH)_4$ arise from excess enthalpies and entropies of the transition states for epoxidation that reflect enthalpically unfavorable interactions between the aliphatic chain of the transition states and water clusters present near $(SiOH)_4$. Within hydrophilic Ti-BEA, clusters of water confined near $(SiOH)_4$ reorganize in response to the formation of transition states for epoxidation, which leads to the rupture of hydrogen bonds and increases in the entropy of these water clusters. However, the apparent activation enthalpies and entropies for H_2O_2 decomposition are not affected by the presence of water because the transition state for H_2O_2 decomposition interacts with these hydrogen-bonded networks in ways similar to Ti–OOH reactive species. These interpretations are consistent with the fact that turnover rates

DOI: 10.1021/jacs.8b12861
J. Am. Chem. Soc. XXXX, XXX, XXX–XXX

for 1-octene epoxidation vary by less than a factor of 2 across the same series of Ti-BEA catalysts when reactions proceed in the absence of water (i.e., using *tert*-butyl hydroperoxide under anhydrous conditions). Epoxidation turnover rates recover their sensitivity to $(SiOH)_4$ groups and exhibit a 20-fold increase with increases in $[(SiOH)_4]$ when small amounts of H_2O were added to the otherwise anhydrous solutions. These data support the conclusion that changes in excess free energies reflect dynamic changes in the structure of water clusters near active sites that result from changes in coverage and molecular structure of the species bound to framework Ti as the reaction proceeds.

Overall, the data and interpretations presented here suggest that the excess free energies of the transition states for liquid-phase reactions within zeolites will be influenced by the density and proximity of $(SiOH)_4$ moieties in the presence of hydrogen-bonding solvents or reactants. Small confined clusters of hydrogen-bond-donating or -accepting molecules (e.g., H_2O or ROH) nucleate at $(SiOH)_4$ and must reorganize to accommodate the adsorption of reactants and the formation of transition states. This solvent reorganization will result in a change in the transition state's excess free energy that is a complex function of the chemical and physical properties of the reactant (e.g., hydrogen-bonding character, and polarity) and of the catalyst (e.g., $(SiOH)_4$ density, pore diameter). The deconvolution of these individual types of interactions and the associated effects on liquid-phase catalysis remain challenging and require a combination of kinetic, spectroscopic, calorimetric, and computational methods; such work represents an important area of research that must be developed to increase understanding of catalysis at solid−liquid interfaces.

■ ASSOCIATED CONTENT

Supporting Information

The Supporting Information is available free of charge on the ACS Publications website at DOI: 10.1021/jacs.8b12861.

Additional catalyst characterization data, solid-state NMR and IR spectroscopic data, partition functions and estimations of entropy, in situ UV−vis spectra of Ti-BEA, additional 1-octene epoxidation kinetics, Polanyi plots, and 1-octene uptake data (PDF)

■ AUTHOR INFORMATION

Corresponding Author

*dwflhrty@illinois.edu

ORCID

Daniel T. Bregante: 0000-0003-2157-1286
Jeffrey Greeley: 0000-0001-8469-1715
Rajamani Gounder: 0000-0003-1347-534X
David W. Flaherty: 0000-0002-0567-8481

Notes

The authors declare no competing financial interest.

■ ACKNOWLEDGMENTS

We thank Ms. Megan Witzke for helpful comments and discussion and Mrs. Giselle Bukowski for her graphical assistance. D.T.B. was supported by the Department of Defense (DoD) through the National Defense Science & Engineering Graduate Fellowship (NDSEG) Program. B.C.B. and J.G. acknowledge support from the NSF DMREF program (CBET-1437219). M.J.C. and R.G. acknowledge support from the Purdue Process Safety and Assurance Center (P2SAC). This work was carried out, in part, in the Frederick Seitz Materials Research Laboratory Central Research Facilities and the School of Chemical Sciences NMR Lab at the University of Illinois. This work was supported by the U.S. Army Research Office under grant number W911NF-18-1-0100, with partial support from a research grant from the National Science Foundation (CBET-15531377).

■ REFERENCES

(1) Bassler, P.; Göbbel, H.; Weidenbach, M. The new HPPO Process for Propylene Oxide: From Joint Development to Worldscale Production. *Chem. End. Trans.* **2010**, *21*, 571−577.

(2) Russo, V.; Tesser, R.; Santacesaria, E.; Di Serio, M. Chemical and Technical Aspects of Propene Oxide Production via Hydrogen Peroxide (HPPO Process). *Ind. Eng. Chem. Res.* **2013**, *52* (3), 1168−1178.

(3) Noh, G.; Shi, Z.; Zones, S. I.; Iglesia, E. Isomerization and β-scission reactions of alkanes on bifunctional metal-acid catalysts: Consequences of confinement and diffusional constraints on reactivity and selectivity. *J. Catal.* **2018**, *368*, 389.

(4) Gounder, R.; Davis, M. E. Monosaccharide and disaccharide isomerization over Lewis acid sites in hydrophobic and hydrophilic molecular sieves. *J. Catal.* **2013**, *308*, 176−188.

(5) Müller, P.; Burt, S. P.; Love, A. M.; McDermott, W. P.; Wolf, P.; Hermans, I. Mechanistic Study on the Lewis Acid Catalyzed Synthesis of 1,3-Butadiene over Ta-BEA Using Modulated Operando DRIFTS-MS. *ACS Catal.* **2016**, *6* (10), 6823−6832.

(6) Corma, A.; Llabrés i Xamena, F. X.; Prestipino, C.; Renz, M.; Valencia, S. Water Resistant, Catalytically Active Nb and Ta Isolated Lewis Acid Sites, Homogeneously Distributed by Direct Synthesis in a Beta Zeolite. *J. Phys. Chem. C* **2009**, *113*, 11306−11315.

(7) Csicsery, S. M. Shape-selective catalysis in zeolites. *Zeolites* **1984**, *4*, 202−213.

(8) Bregante, D. T.; Thornburg, N. E.; Notestein, J. M.; Flaherty, D. W. Consequences of Confinement for Alkene Epoxidation with Hydrogen Peroxide on Highly Dispersed Group 4 and 5 Metal Oxide Catalysts. *ACS Catal.* **2018**, *8*, 2995−3010.

(9) Boronat, M.; Concepción, P.; Corma, A.; Navarro, M. T.; Renz, M.; Valencia, S. Reactivity in the confined spaces of zeolites: the interplay between spectroscopy and theory to develop structure−activity relationships for catalysis. *Phys. Chem. Chem. Phys.* **2009**, *11* (16), 2876−2884.

(10) Gounder, R.; Iglesia, E. The catalytic diversity of zeolites: confinement and solvation effects within voids of molecular dimensions. *Chem. Commun. (Cambridge, U. K.)* **2013**, *49* (34), 3491−509.

(11) Kosinov, N.; Liu, C.; Hensen, E. J. M.; Pidko, E. A. Engineering of Transition Metal Catalysts Confined in Zeolites. *Chem. Mater.* **2018**, *30* (10), 3177−3198.

(12) Cordon, M. J.; Harris, J. W.; Vega-Vila, J. C.; Bates, J. S.; Kaur, S.; Gupta, M.; Witzke, M E.; Wegener, E. C.; Miller, J. T.; Flaherty, D. W.; Hibbitts, D. D.; Gounder, R. The Dominant Role of Entropy in Stabilizing Sugar Isomerization Transition States within Hydrophobic Zeolite Pores. *J. Am. Chem. Soc.* **2018**, *140*, 14244−14266.

(13) Farzaneh, A.; DeJaco, R. F.; Ohlin, L.; Holmgren, A.; Siepmann, J. I.; Grahn, M. Comparative Study of the Effect of Defects on Selective Adsorption of Butanol from Butanol/Water Binary Vapor Mixtures in Silicalite-1 Films. *Langmuir* **2017**, *33* (34), 8420−8427.

(14) Gounder, R. Hydrophobic microporous and mesoporous oxides as Brønsted and Lewis acid catalysts for biomass conversion in liquid water. *Catal. Sci. Technol.* **2014**, *4*, 2877−2886.

(15) Oyama, S. T. Rates, Kinetics, and Mechanisms of Epoxidation. In *Mechanisms in Homogeneous and Heterogeneous Epoxidation Catalysis*; Elsevier: 2008; pp 3−99.

DOI: 10.1021/jacs.8b12861
J. Am. Chem. Soc. XXXX, XXX, XXX−XXX

(16) Yadav, A.; Jackson, R. M.; Holbrook, J. J.; Warshel, A. Role of Solvent Reorganization Energies in the Catalytic Activity of Enzymes. *J. Am. Chem. Soc.* **1991**, *113*, 4800−4805.
(17) Reichardt, D.; Welton, T. *Solvents and Solvent Effects in Organic Chemistry*, 4th ed.; Wiley-VCH: 2010.
(18) Sievers, C.; Noda, Y.; Qi, L.; Albuquerque, E. M.; Rioux, R. M.; Scott, S. L. Phenomena Affecting Catalytic Reactions at Solid−Liquid Interfaces. *ACS Catal.* **2016**, *6* (12), 8286−8307.
(19) Research Areas: Catalysis Science. https://science.energy.gov/bes/csgb/research-areas/catalysis-science/ (accessed August 8, 2018).
(20) Dartt, C. B.; Davis, M. E. Characterization and catalytic activity of titanium containing SSZ-33 and aluminum-free zeolite beta. *Appl. Catal., A* **1996**, *143*, 53−73.
(21) Khouw, C. B.; Dartt, C. B.; Labinger, J. A.; Davis, M. E. Studies on the Catalytic Oxidation of Alkanes and Alkenes by Titanium Silicates. *J. Catal.* **1994**, *149*, 195−205.
(22) Corma, A.; Esteve, P.; Martínez, A. Solvent Effects during the Oxidation of Olefins and Alcohols with Hydrogen Peroxide on Ti-Beta Catalyst: The Influence of the Hydrophilicity-Hydrophobicity of the Zeolite. *J. Catal.* **1996**, *161*, 11−19.
(23) Goldsmith, B. R.; Hwang, T.; Seritan, S.; Peters, B.; Scott, S. L. Rate-Enhancing Roles of Water Molecules in Methyltrioxorhenium-Catalyzed Olefin Epoxidation by Hydrogen Peroxide. *J. Am. Chem. Soc.* **2015**, *137* (30), 9604−9616.
(24) Wang, L.; Sun, J.; Meng, X.; Zhang, W.; Zhang, J.; Pan, S.; Shen, Z.; Xiao, F. S. A significant enhancement of catalytic activities in oxidation with H_2O_2 over the TS-1 zeolite by adjusting the catalyst wettability. *Chem. Commun. (Cambridge, U. K.)* **2014**, *50* (16), 2012−2014.
(25) Vega-Vila, J. C.; Harris, J. W.; Gounder, R. Controlled insertion of tin atoms into zeolite framework vacancies and consequences for glucose isomerization catalysis. *J. Catal.* **2016**, *344*, 108−120.
(26) Bhan, A.; Gounder, R.; Macht, J.; Iglesia, E. Entropy considerations in monomolecular cracking of alkanes on acidic zeolites. *J. Catal.* **2008**, *253* (1), 221−224.
(27) Conrad, S.; Wolf, P.; Müller, P.; Orsted, H.; Hermans, I. Influence of Hydrophilicity on the Snβ-Catalyzed Baeyer-Villiger Oxidation of Cyclohexanone with Aqueous Hydrogen Peroxide. *ChemCatChem* **2017**, *9* (1), 175−182.
(28) Trzpit, M.; Soulard, M.; Patarin, J.; Desbiens, N.; Cailliez, F.; Boutin, A.; Demachy, I.; Fuchs, A. H. The Effect of Local Defects on Water adsorption in Silicalite-1 Zeolite: A Joint Experimental and Molecular Simulation Study. *Langmuir* **2007**, *23*, 10131−10139.
(29) Zhang, K.; Lively, R. P.; Noel, J. D.; Dose, M. E.; McCool, B. A.; Chance, R. R.; Koros, W. J. Adsorption of water and ethanol in MFI-type zeolites. *Langmuir* **2012**, *28* (23), 8664−8673.
(30) Özgür Yazaydın, A.; Thompson, R. W. Molecular simulation of water adsorption in silicalite: Effect of silanol groups and different cations. *Microporous Mesoporous Mater.* **2009**, *123* (1−3), 169−176.
(31) Nguyen, V. T.; Nguyen, P. T. M.; Dang, L. X.; Mei, D.; Wick, C. D.; Do, D. D. A comparative study of the adsorption of water and methanol in zeolite BEA: a molecular simulation study. *Mol. Simul.* **2014**, *40* (14), 1113−1124.
(32) Bai, P.; Tsapatsis, M.; Siepmann, J. I. Multicomponent adsorption of alcohols onto silicalite-1 from aqueous solution: isotherms, structural analysis, and assessment of ideal adsorbed solution theory. *Langmuir* **2012**, *28* (44), 15566−15576.
(33) Clerici, M. G. The activity of titanium silicalite-1 (TS-1): Some considerations on its origin. *Kinet. Catal.* **2015**, *56* (4), 450−455.
(34) Gounder, R.; Davis, M. E. Beyond shape selective catalysis with zeolites: Hydrophobic void spaces in zeolites enable catalysis in liquid water. *AIChE J.* **2013**, *59* (9), 3349−3358.
(35) Wu, L.; Tang, Z.; Yu, Y.; Yao, X.; Liu, W.; Li, L.; Yan, B.; Liu, Y.; He, M. Facile synthesis of a high-performance titanosilicate catalyst with controllable defective Ti(OSi)3OH sites. *Chem. Commun. (Cambridge, U. K.)* **2018**, *54* (49), 6384−6387.
(36) Blasco, T.; Camblor, M. A.; Corma, A.; Esteve, P.; Guil, J. M.; Martinez, A.; Perdigon-Melon, J. A.; Valencia, S. Direct synthesis and characterization of hydrophobic aluminum-free Ti-beta zeolite. *J. Phys. Chem. B* **1998**, *102*, 75−88.
(37) Ge, T.; Hua, Z.; Lv, J.; Zhou, J.; Guo, H.; Zhou, J.; Shi, J. Hydrophilicity/hydrophobicity modulated synthesis of nano-crystalline and hierarchically structured TS-1 zeolites. *CrystEngComm* **2017**, *19* (10), 1370−1376.
(38) Park, S.; Cho, K. M.; Youn, M. H.; Seo, J. G.; Jung, J. C.; Baeck, S.-H.; Kim, T. J.; Chung, Y.-M.; Oh, S.-H.; Song, I. K. Direct epoxidation of propylene with hydrogen peroxide over TS-1 catalysts: Effect of hydrophobicity of the catalysts. *Catal. Commun.* **2008**, *9* (15), 2485−2488.
(39) Chorkendorff, I.; Niemantsverdriet, J. W. H. *Concepts of Modern Catalysis and Kinetics*, 2nd ed.; Wiley-VCH Verlag Gmbh & Co.: Weinheim, Germany, 2007.
(40) Madon, R. J.; Boudart, M. Experimental Criterion for the Absence of Artifacts in the Measurement of Rates of Heterogeneous Catalytic Reactions. *Ind. Eng. Chem. Fundam.* **1982**, *21*, 438−447.
(41) Grosso-Giordano, N. A.; Schroeder, C.; Okrut, A.; Solovyov, A.; Schottle, C.; Chasse, W.; Marinkovic, N.; Koller, H.; Zones, S. I.; Katz, A. Outer-Sphere Control of Catalysis on Surfaces: A Comparative Study of Ti(IV) Single-Sites Grafted on Amorphous versus Crystalline Silicates for Alkene Epoxidation. *J. Am. Chem. Soc.* **2018**, *140* (15), 4956−4960.
(42) Bregante, D. T.; Priyadarshini, P.; Flaherty, D. W. Kinetic and spectroscopic evidence for reaction pathways and intermediates for olefin epoxidation on Nb in * BEA. *J. Catal.* **2017**, *348*, 75−89.
(43) Bregante, D. T.; Flaherty, D. W. Periodic Trends in Olefin Epoxidation over Group IV and V Framework Substituted Zeolite Catalysts: A Kinetic and Spectroscopic Study. *J. Am. Chem. Soc.* **2017**, *139* (20), 6888−6898.
(44) Dzwigaj, S.; Millot, Y.; Che, M. Ta(V)-Single Site BEA Zeolite by Two-Step Postsynthesis Method: Preparation and Characterization. *Catal. Lett.* **2010**, *135* (3−4), 169−174.
(45) Dzwigaj, S.; Millot, Y.; Méthivier, C.; Che, M. Incorporation of Nb(V) into BEA zeolite investigated by XRD, NMR, IR, DR UV−vis, and XPS. *Microporous Mesoporous Mater.* **2010**, *130* (1−3), 162−166.
(46) Tang, B.; Dai, W.; Sun, X.; Guan, N.; Li, L.; Hunger, M. A procedure for the preparation of Ti-Beta zeolites for catalytic epoxidation with hydrogen peroxide. *Green Chem.* **2014**, *16* (4), 2281−2291.
(47) Wolf, P.; Hammond, C.; Conrad, S.; Hermans, I. Post-synthetic preparation of Sn-, Ti- and Zr-beta: a facile route to water tolerant, highly active Lewis acidic zeolites. *Dalton Trans* **2014**, *43* (11), 4514−4519.
(48) Wang, J.; Kispersky, V. F.; Nicholas Delgass, W.; Ribeiro, F. H. Determination of the Au active site and surface active species via operando transmission FTIR and isotopic transient experiments on 2.3wt.% Au/TiO2 for the WGS reaction. *J. Catal.* **2012**, *289*, 171−178.
(49) Kresse, G.; Hafner, J. Ab initiomolecular-dynamics simulation of the liquid-metal−amorphous-semiconductor transition in germanium. *Phys. Rev. B: Condens. Matter Mater. Phys.* **1994**, *49* (20), 14251−14269.
(50) Kresse, G.; Furthmüller, J. Efficient iterative schemes for ab initio total-energy calculations using a plane-wave basis set. *Phys. Rev. B: Condens. Matter Mater. Phys.* **1996**, *54*, 11169−11184.
(51) Kresse, G.; Furthmüller, J. Efficiency of ab-initio total energy calculations for metals and semiconductors using a plane-wave basis set. *Comput. Mater. Sci.* **1996**, *6*, 15−50.
(52) Kresse, G.; Hafner, J. Ab initio molecular dynamics for liquid metals. *Phys. Rev. B: Condens. Matter Mater. Phys.* **1993**, *47* (1), 558−561.
(53) Bukowski, B. C.; Bates, J. S.; Gounder, R.; Greeley, J. First principles, microkinetic, and experimental analysis of Lewis acid site speciation during ethanol dehydration on Sn-Beta zeolites. *J. Catal.* **2018**, *365*, 261−276.
(54) Blöchl, P. E. Projector augmented-wave method. *Phys. Rev. B: Condens. Matter Mater. Phys.* **1994**, *50* (24), 17953−17979.

DOI: 10.1021/jacs.8b12861
J. Am. Chem. Soc. XXXX, XXX, XXX−XXX

(55) Kresse, G.; Joubert, D. From ultrasoft pseudopotentials to the projector augmented-wave method. *Phys. Rev. B: Condens. Matter Mater. Phys.* **1999**, *59*, 1758−1775.
(56) Wellendorff, J.; Lundgaard, K. T.; Møgelhøj, A.; Petzold, V.; Landis, D. D.; Nørskov, J. K.; Bligaard, T.; Jacobsen, K. W. Density functionals for surface science: Exchange-correlation model development with Bayesian error estimation. *Phys. Rev. B: Condens. Matter Mater. Phys.* **2012**, *85* (23), 235149.
(57) Baerlocher, C.; McCusker, L. B. *Database of Zeolite Structures*. http://www.iza-structure.org/databases/.
(58) Lin, S.-T.; Maiti, P. K.; Goddard, W. A. Two-Phase Thermodynamic Model for Efficient and Accurate Absolute Entropy of Water from Molecular Dynamics Simulations. *J. Phys. Chem. B* **2010**, *114*, 8191−8198.
(59) Lin, S.-T.; Blanco, M.; Goddard, W. A. The two-phase model for calculating thermodynamic properties of liquids from molecular dynamics: Validation for the phase diagram of Lennard-Jones fluids. *J. Chem. Phys.* **2003**, *119* (22), 11792−11805.
(60) Pascal, T. A.; Lin, S. T.; Goddard, W. A., 3rd Thermodynamics of liquids: standard molar entropies and heat capacities of common solvents from 2PT molecular dynamics. *Phys. Chem. Chem. Phys.* **2011**, *13* (1), 169−81.
(61) Brehm, M.; Kirchner, B. TRAVIS - a free analyzer and visualizer for Monte Carlo and molecular dynamics trajectories. *J. Chem. Inf. Model.* **2011**, *51* (8), 2007−23.
(62) Alexopoulos, K.; Lee, M.-S.; Liu, Y.; Zhi, Y.; Liu, Y.; Reyniers, M.-F.; Marin, G. B.; Glezakou, V.-A.; Rousseau, R.; Lercher, J. A. Anharmonicity and Confinement in Zeolites: Structure, Spectroscopy, and Adsorption Free Energy of Ethanol in H-ZSM-5. *J. Phys. Chem. C* **2016**, *120* (13), 7172−7182.
(63) Thornburg, N. E.; Thompson, A. B.; Notestein, J. M. Periodic Trends in Highly Dispersed Groups IV and V Supported Metal Oxide Catalysts for Alkene Epoxidation with H_2O_2. *ACS Catal.* **2015**, *5* (9), 5077−5088.
(64) Klaas, J.; Schulz-Ekloff, G.; Jaeger, N. I. UV-Visible Diffuse Reflectance Spectroscopy of Zeolite-Hosted Mononuclear Titanium Oxide Species. *J. Phys. Chem. B* **1997**, *101*, 1305−1311.
(65) Prodinger, S.; Shi, H.; Eckstein, S.; Hu, J. Z.; Olarte, M. V.; Camaioni, D. M.; Derewinski, M. A.; Lercher, J. A. Stability of Zeolites in Aqueous Phase Reactions. *Chem. Mater.* **2017**, *29*, 7255−7262.
(66) Prodinger, S.; Derewinski, M. A.; Vjunov, A.; Burton, S. D.; Arslan, I.; Lercher, J. A. Improving Stability of Zeolites in Aqueous Phase via Selective Removal of Structural Defects. *J. Am. Chem. Soc.* **2016**, *138* (13), 4408−4415.
(67) Hadjiivanov, K.; Ivanova, E.; Kefirov, R.; Janas, J.; Plesniar, A.; Dzwigaj, S.; Che, M. Adsorption properties of Fe-containing dealuminated BEA zeolites as revealed by FTIR spectroscopy. *Microporous Mesoporous Mater.* **2010**, *131* (1−3), 1−12.
(68) Bordiga, S.; Lamberti, C.; Bonino, F.; Travert, A.; Thibault-Starzyk, F. Probing zeolites by vibrational spectroscopies. *Chem. Soc. Rev.* **2015**, *44* (20), 7262−7341.
(69) Sayed, M. B.; Kydd, R. A.; Cooney, R. P. A Fourier-Transform Infrared Spectral Study of H-ZSM-5 Surface Sites and Reactivity Sequences in Methanol Conversion. *J. Catal.* **1984**, *88*, 137−149.
(70) Shields, R. M.; Temelso, B.; Archer, K. A.; Morrell, T. E.; Shields, G. C. Accurate Predictions of Water Cluster Formation, $(H_2O)n$ = 2−10. *J. Phys. Chem. A* **2010**, *114*, 11725−11737.
(71) Harris, J. W.; Cordon, M. J.; Di Iorio, J. R.; Vega-Vila, J. C.; Ribeiro, F. H.; Gounder, R. Titration and quantification of open and closed Lewis acid sites in Sn-Beta zeolites that catalyze glucose isomerization. *J. Catal.* **2016**, *335*, 141−154.
(72) Sushkevich, V. L.; Vimont, A.; Travert, A.; Ivanova, I. I. Spectroscopic Evidence for Open and Closed Lewis Acid Sites in ZrBEA Zeolites. *J. Phys. Chem. C* **2015**, *119* (31), 17633−17639.
(73) Fawcett, W. R.; Liu, G.; Kessler, T. E. Solvent-Induced Frequency Shifts in the Infrared Spectrum of Acetonitrile in Organic Solvents. *J. Phys. Chem.* **1993**, *97*, 9293−9298.
(74) Campbell, C. T.; Sellers, J. R. The entropies of adsorbed molecules. *J. Am. Chem. Soc.* **2012**, *134* (43), 18109−18115.
(75) Denmark, S. E.; Beutner, G. L. Lewis base catalysis in organic synthesis. *Angew. Chem., Int. Ed.* **2008**, *47* (9), 1560−638.
(76) Hogg, J. M.; Brown, L. C.; Matuszek, K.; Latos, P.; Chrobok, A.; Swadzba-Kwasny, M. Liquid coordination complexes of Lewis acidic metal chlorides: Lewis acidity and insights into speciation. *Dalton Trans* **2017**, *46* (35), 11561−11574.
(77) Gates, B. C.; Knoezinger, H.; Jentoft, F. C. *Advances in Catalysis*; Academic Press: 2011; Vol. *54*.
(78) Anslyn, E. V.; Dougherty, D. A. *Modern Physical Organic Chemistry*; University Science: 2005.
(79) Ivanchikova, I. D.; Skobelev, I. Y.; Maksimchuk, N. V.; Paukshtis, E. A.; Shashkov, M. V.; Kholdeeva, O. A. Toward understanding the unusual reactivity of mesoporous niobium silicates in epoxidation of C C bonds with hydrogen peroxide. *J. Catal.* **2017**, *356*, 85−99.
(80) Yoon, C. W.; Hirsekorn, K. F.; Neidig, M. L.; Yang, X.; Tilley, T. D. Mechanism of the Decomposition of Aqueous Hydrogen Peroxide over Heterogeneous TiSBA15 and TS-1 Selective Oxidation Catalysts: Insights from Spectroscopic and Density Functional Theory Studies. *ACS Catal.* **2011**, *1* (12), 1665−1678.
(81) Ruddy, D. A.; Tilley, T. D. Kinetics and Mechanism of Olefin Epoxidation with Aqueous H_2O_2 and a Highly Selective Surface-Modified TaSBA15 Heterogeneous Catalyst. *J. Am. Chem. Soc.* **2008**, *130*, 11088−11096.
(82) Bonino, F.; Damin, A.; Ricchiardi, G.; Ricci, M.; Spanó, G.; D'Aloisio, R.; Zecchina, A.; Lamberti, C.; Prestipino, C.; Bordiga, S. Ti-Peroxo Species in the Ts-1/H_2O_2/H_2O System. *J. Phys. Chem. B* **2004**, *108*, 3573−3583.
(83) Bordiga, S.; Damin, A.; Bonino, F.; Ricchiardi, G.; Lamberti, C.; Zecchina, A. The Structure of the Peroxo Species in the TS-1 Catalyst as Investigated by Resonant Raman Spectroscopy. *Angew. Chem., Int. Ed.* **2002**, *41*, 4734−4737.
(84) Corma, A.; Camblor, M. A.; Esteve, P.; Martínez, A.; Perez-Pariente, J. Activity of Ti-Beta Catalyst for the Selective Oxidation of Alkenes and Alkanes. *J. Catal.* **1994**, *145*, 151−158.
(85) Bregante, D. T.; Patel, A. Y.; Johnson, A. M.; Flaherty, D. W. Catalytic Thiophene Oxidation by Groups 4 and 5 Framework-Substituted Zeolites with Hydrogen Peroxide: Mechanistic and Spectroscopic Evidence for the Effects of Metal Lewis Acidity and Solvent Lewis Basicity. *J. Catal.* **2018**, *364*, 415−425.
(86) Bordiga, S.; Groppo, E.; Agostini, G.; van Bokhoven, J. A.; Lamberti, C. Reactivity of surface species in heterogeneous catalysts probed by in situ X-ray absorption techniques. *Chem. Rev.* **2013**, *113* (3), 1736−1850.
(87) Stare, J.; Henson, N. J.; Eckert, J. Mechanistic Aspects of Propene Epoxidation by Hydrogen Peroxide. Catalytic Role of Water Molecules, External Electric Field, and Zeolite Framework of TS-1. *J. Chem. Inf. Model.* **2009**, *49*, 833−846.
(88) Clerici, M. G.; Ingallina, P. Epoxidation of Lower Olefins with Hydrogen Peroxide and Titanium Silicalite. *J. Catal.* **1993**, *140*, 71−83.
(89) Kurti, L.; Czako, B. *Strategic Applications of Named Reactions in Organic Synthesis*; Academic Press: 2005.
(90) Deubel, D. V.; Sundermeyer, J.; Frenking, G. Mechanism of the Olefin Epoxidation Catalyzed by Molybdenum Diperoxo Complexes: Quantum-Chemical Calculations Give an Answer to a Long-Standing Question. *J. Am. Chem. Soc.* **2000**, *122*, 10101−10108.
(91) Kuznetsov, M. L.; Pessoa, J. C. Epoxidation of olefins catalysed by vanadium-salan complexes: a theoretical mechanistic study. *Dalton Trans* **2009**, No. 28, 5460−5468.
(92) Wang, L.; Xiong, G.; Su, J.; Li, P.; Guo, H. In Situ UV Raman Spectroscopic Study on the Reaction Intermediates for Propylene Epoxidation on TS-1. *J. Phys. Chem. C* **2012**, *116* (16), 9122−9131.
(93) Xiong, G.; Cao, Y.; Guo, Z.; Jia, Q.; Tian, F.; Liu, L. The roles of different titanium species in TS-1 zeolite in propylene epoxidation studied by in situ UV Raman spectroscopy. *Phys. Chem. Chem. Phys.* **2016**, *18* (1), 190−196.

DOI: 10.1021/jacs.8b12861
J. Am. Chem. Soc. XXXX, XXX, XXX−XXX

(94) Brutchey, R. L.; Ruddy, D. A.; Andersen, L. K.; Tilley, T. D. Influence of Surface Modification of Ti-SBA15 Catalysts on the Epoxidation Mechanism for Cyclohexene with Aqueous Hydrogen Peroxide. *Langmuir* **2005**, *21*, 9576−9583.
(95) Ruddy, D. A.; Brutchey, R. L.; Tilley, T. D. The Influence of Surface Modification on the Epoxidation Selectivity and Mechanism of TiSBA15 and TaSBA15 Catalysts with Aqueous Hydrogen Peroxide. *Top. Catal.* **2008**, *48* (1−4), 99−106.
(96) Madon, R. J.; Iglesia, E. Catalytic reaction rates in thermodynamically non-ideal systems. *J. Mol. Catal. A: Chem.* **2000**, *163*, 189−204.
(97) Sever, R. R.; Root, T. W. DFT Study of Solvent Coordination Effects on Titanium-Based Epoxidation Catalysts. Part Two: Reactivity of Titanium Hydroperoxo Complexes in Ethylene Epoxidation. *J. Phys. Chem. B* **2003**, *107*, 4090−4099.
(98) Panyaburapa, W.; Nanok, T.; Limtrakul, J. L. Epoxidation Reaction of Unsaturated Hydrocarbons with H2O2 over Defect TS-1 Investigated by ONIOM Method: Formation of Active Sites and Reaction Mechanisms. *J. Phys. Chem. C* **2007**, *111*, 3433−3441.
(99) Chandler, D. Interfaces and the driving force of hydrophobic assembly. *Nature* **2005**, *437* (7059), 640−647.
(100) Striolo, A. Chapter 10: Nano-confined water. *Theor. Comput. Chem.* **2007**, *18*, 245−274.
(101) Munoz-Santiburcio, D.; Marx, D. Chemistry in nanoconfined water. *Chem. Sci.* **2017**, *8* (5), 3444−3452.
(102) Silverstein, K. A. T.; Haymet, A. D. J.; Dill, K. A. The Strength of Hydrogen Bonds in Liquid Water and Around Nonpolar Solutes. *J. Am. Chem. Soc.* **2000**, *122*, 8037−8041.
(103) Walrafen, G. E.; Chu, Y. C. Shear Viscosity, Heat Capacity, and Fluctuations of Liquid Water, All at Constant Molal Volume. *J. Phys. Chem.* **1991**, *95*, 8909−8921.
(104) Zhu, Z.; Xu, H.; Jiang, J.; Wu, H.; Wu, P. Structural reconstruction: a milestone in the hydrothermal synthesis of highly active Sn-Beta zeolites. *Chem. Commun. (Cambridge, U. K.)* **2017**, *53* (93), 12516−12519.
(105) Corma, A.; Nemeth, L.; Renz, M.; Valencia, S. Sn-zeolite beta as a heterogeneous chemoselective catalytic for Baeyer-Villiger oxidations. *Nature* **2001**, *412*, 423−425.
(106) Wang, J.; Okumura, K.; Jaenicke, S.; Chuah, G.-K. Post-synthesized zirconium-containing Beta zeolite in Meerwein−Ponndorf−Verley reduction: Pros and cons. *Appl. Catal., A* **2015**, *493*, 112−120.
(107) Moteki, T.; Rowley, A. T.; Bregante, D. T.; Flaherty, D. W. Formation Pathways toward 2- and 4-Methylbenzaldehyde via Sequential Reactions from Acetaldehyde over Hydroxyapatite Catalyst. *ChemCatChem* **2017**, *9* (11), 1921−1929.
(108) Wu, P.; Tatsumi, T. Preparation of B-free Ti-MWW through reversible structural conversion. *Chem. Commun.* **2002**, *10*, 1026−1027.

DOI: 10.1021/jacs.8b12861
J. Am. Chem. Soc. XXXX, XXX, XXX−XXX